ΕΘΝΙΚΟ & ΚΑΠΟΔΙΣΤΡΙΑΚΟ ΠΑΝΕΠΙΣΤΗΜΙΟ ΑΘΗΝΩΝ
ΣΧΟΛΗ ΕΠΙΣΤΗΜΩΝ ΥΓΕΙΑΣ
ΤΜΗΜΑ ΙΑΤΡΙΚΗΣ
ΔΠΜΣ ΙΑΤΡΙΚΗ ΦΥΣΙΚΗ - ΑΚΤΙΝΟΦΥΣΙΚΗ

ΔΙΠΛΩΜΑΤΙΚΗ ΕΡΓΑΣΙΑ:

Ποσοτική ανάλυση της πρόσληψης ^{68}Ga-DOTATOC PET/CT στην υπόφυση και τα επινεφρίδια με την χρήση χαρακτηριστικών υφής και δεικτών SUV

Κωνσταντινίδη Νικολέττα

ΑΜ: 7450132200014

Ακαδημαϊκός Επιβλέπων: Μεταξάς Μαρίνος

Αθήνα 2024

ΕΘΝΙΚΟ & ΚΑΠΟΔΙΣΤΡΙΑΚΟ ΠΑΝΕΠΙΣΤΗΜΙΟ ΑΘΗΝΩΝ
ΣΧΟΛΗ ΕΠΙΣΤΗΜΩΝ ΥΓΕΙΑΣ
ΤΜΗΜΑ ΙΑΤΡΙΚΗΣ
ΔΠΜΣ ΙΑΤΡΙΚΗ ΦΥΣΙΚΗ - ΑΚΤΙΝΟΦΥΣΙΚΗ

THESIS:

Quantitative analysis of ^{68}Ga-DOTATOC PET/CT uptake in the pituitary and adrenal glands using textural features and SUV indices

Konstantinidi Nikoletta

AM: 7450132200014

Academic Supervisor: Metaxas Marinos

Athens 2024

Acknowledgements

I would like to express my gratitude to my Academic supervisor, the Medical Physicist of BRFAA, Dr.Marinos Metaxas, for his invaluable patience, feedback, and clinical expertise, which greatly contributed to our research. I am also thankful to the Research Professors from the Mathematics Research Center of the Academy of Athens, Dr.Nikolaos Dikaios and Dr.George Kastis, for their moral support, assistance in result analysis, and generation of ideas throughout the course of the investigation. Finally, I extend my thanks to Prof.Pantelis Karaiskos, Director and Professor at the Laboratory of Medical Physics of the NKUA, for providing me with the opportunity to collaborate with the scientists of the Academy of Athens.

Abstract

Σκοπός της παρούσας μελέτης είναι η ποσοτικοποίηση της έκφρασης των φυσιολογικών υποδοχέων σωματοστατίνης (SSTR2) με τη χρήση της μέσης κανονικοποιημένης τιμής απορρόφησης (SUV_{mean}) του ^{68}Ga-DOTA(0)-Phe(1)-Tyr(3)-octreotide (DOTATOC), σε ασθενείς που υποβάλλονται σε Τομογραφία Εκπομπής Ποζιτρονίων (PET)/ Υπολογιστική Τομογραφία (CT). Η έρευνα αυτή διεξάγεται στην υπόφυση και τα επινεφρίδια (φυσιολογικοί υποδοχείς) με γαστρεντεροπαγκρεατικούς-νευροενδοκρινείς όγκους (GEP-NETs). Η μελέτη επικεντρώνεται στην ανάλυση των μετρήσεων του δείκτη SUV και των ραδιομικών χαρακτηριστικών της εικόνας, για να προσφέρει ποσοτική κατανόηση της απόκρισης των υποδοχέων σωματοστατίνης της υπόφυσης του εγκεφάλου και των επινεφριδίων. Τα δεδομένα συλλέχθηκαν από ασθενείς που υποβλήθηκαν σε εξέταση ^{68}Ga-DOTATOC PET/CT στο μηχάνημα SIEMENS Biograph Vision-450 PET/CT στο Ίδρυμα Ιατροβιολογικών Ερευνών της Ακαδημίας Αθηνών (IIBEAA). Οι μετρήσεις πρόσληψης πραγματοποιήθηκαν με τη χρήση του λογισμικού LIFEx-7.4.0 για τον υπολογισμό των δεικτών SUV και των χαρακτηριστικών υφής σε κάθε περιοχή ενδιαφέροντος. Οι δείκτες $SUVmax$ και $SUVmean$ δεν φαίνεται να έχουν καμία συσχέτιση με το σωματικό βάρος του ασθενούς ή την χορηγούμενη δόση. Αντίθετα, δείχνουν μεγάλη συσχέτιση με τον συντελεστή Παραλλακτικότητας (COV) του $SUVmean$ που εκφράζει την ετερογένεια των υποδοχέων. Με βάση τη μικρή τυπική απόκλιση του συντελεστή COV και τον παρατηρούμενο μέσο όρο του SUV_{mean} που έχει τιμή περίπου 3 στην υπόφυση και περίπου 9 στα επινεφρίδια, αντικατοπτρίζονται σταθερά και φυσιολογικά επίπεδα απορρόφησης, υποδεικνύοντας μια σταθερότητα στον αριθμό των πεπτιδικών υποδοχέων και για τις δυο ανατομικές περιοχές. Η κατανόηση αυτών των επιπέδων αναφοράς είναι απαραίτητη για τη διαφοροποίηση της φυσιολογικής από την παθολογική πρόσληψη. Τέλος, έχει σημαντικές κλινικές επιπτώσεις για τη δοσιμετρική ανάλυση των σχετικών ραδιοθεραπευτικών διαδικασιών (π.χ. ^{177}Lu-DOTATOC).

Abstract

The aim of this study is to quantify the expression of the somatostatin physiological receptors (SSTR2) using the mean standardized uptake value ($SUVmean$) of ^{68}Ga-DOTA(0)-Phe(1)-Tyr(3)-octreotide (DOTATOC), in patients undergoing Positron Emission Tomography(PET)/Computed Tomography (CT). This investigation is conducted in the pituitary and adrenal glands (physiological receptors) with gastroenteropancreatic-neuroendocrine tumors (GEP-NETs). The study focuses on analyzing the SUV index measurements and the radiomic characteristics of the image, with the aim of providing quantitative insight into the response of the pituitary receptors in the brain and the adrenal glands. Data were collected from patients undergoing ^{68}Ga-DOTATOC PET/CT examination on the SIEMENS Biograph Vision-450 PET/CT at the Biomedical Research Foundation Academy of Athens (BRFAA). Uptake measurements were performed using LIFEx-7.4.0 software to calculate the SUV indices and to extract the textural features in each region of interest. The results represent a quantitative report on the uptake of ^{68}Ga-DOTATOC, examining the values of $SUVmax$ and $SUVmean$. The SUV indices appear to have no correlation with the body weight of the patient or the injected activity. On the contrary, they show a strong correlation with the Coefficient of Variation (COV), which expresses the heterogeneity of the receptors. Based on the small standard deviation of the COV and the observed $SUVmean$ which has a value of approximately 3 in the pituitary gland and around 9 in the adrenal glands, consistent and physiological uptake levels within these structures are reflected, indicating a stability in the number of peptide receptors for both anatomical areas. Understanding these baseline values is essential for distinguishing normal from pathological uptake and holds significant clinical implications for dosimetric analysis of the related radio-therapeutic procedures (i.e. ^{177}Lu-DOTATOC).

Contents

Introduction

Part I

Theoretical section

Chapter 1

PET-Positron Emission Tomography

Positron emission tomography (PET) is a technique used in clinical medicine and biomedical research, creating images that depict anatomical structures, as well as molecular imaging that reveals the physiological functions of tissues, providing insight into how these tissues perform. It is mostly used for in vivo measurements of metabolism in normal or abnormal tissues.

PET imaging is a field of Nuclear Medicine. Nuclear Medicine is the medical specialty consisting of diagnostic and therapeutic procedures that require the introduction of radioactivity into the body by intravenous injection, inhalation or ingestion[1].

1.1 PET Imaging

The procedure begins with the calculation of the administered dose to the examinee. A radiopharmaceutical is introduced into the patient's body, which participates in normal body processes, and is labelled with short-lived radionuclides. These radionuclides emits positrons (b^+ particles) with a significant kinetic energy (100s keV), they interact with matter and lose energy. When the kinetic energy decreases (close to 0) they are annihilated by the electrons in the tissue. Each annihilation produces two diametrically opposed photons with high-energy of 511 keV each, which can be detected externally. Photons are detected externally by radiation detectors connected to an appropriate coincidence circuit [1].

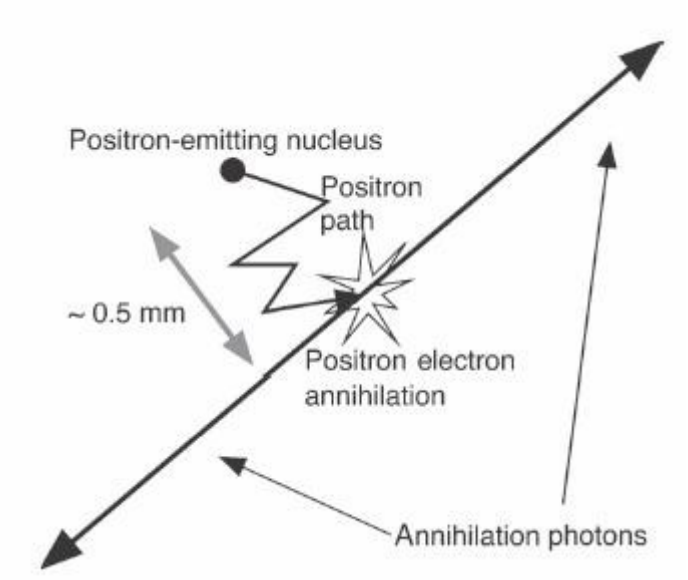

Figure 1.1: PET measures the two annihilated photons produced simultaneously after positron emission from a radionuclide-tagged tracer molecule, chosen to mark a specific function in the body at a biochemical level. Source: radiologykey.com

1.1.1 The Physics of PET/CT

1.1.2 Beta decay

Beta decay is a consequence of the weak force, which is characterized by relatively lengthy decay times. An atomic nucleus is transmuted into another nucleus either with an atomic number increased by one and emitting a β^- particle, i.e. an electron (e^-), in which case the decay is given a special name β^- decay. Or with an atomic number decreased by one and emitting a β^+ particle, i.e. a positron (e^+), in which case the decay is given the special name β^+ decay. In addition to these basic decays, there are also those of $\beta\beta$ decay in which two β particles are emitted simultaneously and an e^- capture in which an orbital electron is captured. In all these reactions the mass number of the nucleus remains constant [1].

$$p = n + e^+ + \nu_e \ , \tag{1.1}$$

$$(Z, A) = (Z - 1, A) + e^+ + \nu_e + E \ . \tag{1.2}$$

As depicted in the figure below,

- β particles emit energy from zero (0) to E_{max} with an $E_{mean} = 1/3E_{max}$.

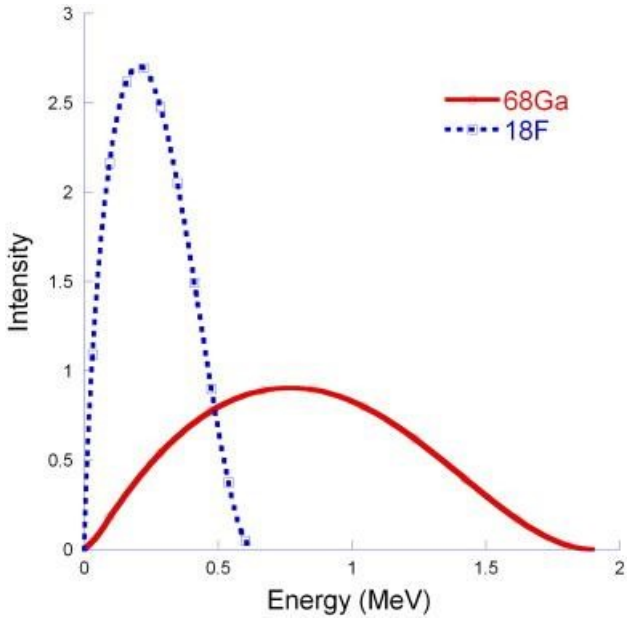

Figure 1.2: Positron Kinetic Energy of Gallium-68 and Fluorine-18, Source: ScienceDirect.com

- The spectrum of β particles is continuous due to the presence of neutrino, since the energy is distributed equally between the positron, the neutrino and the daughter nucleus.

1.1.3 Pair Production

Pair production occurs when a photon has at least the minimum energy (threshold energy) required to create two particles. This threshold energy must be equal to twice the rest energy of an electron, as it is needed to produce both an electron and a positron.

$$2m_e \cdot c^2 = 2 \cdot 0.511MeV = 1.022MeV \ . \tag{1.3}$$

The interaction takes place between the photon and the nucleus of the atom. The result of this interaction is the disappearance of the photon. An electron and a positron appear in its place. In this case we have the conversion of energy (photon) into mass (electron and positron). The electron and positron will transmit their energy to the material by excitation and ionization. However, at the end of its orbit the positron will interact with an electron in the material and they will annihilate. They will disappear and two photons will appear in their place.

$$e^+ + e^- \Rightarrow \gamma + \gamma \ . \tag{1.4}$$

Here we have the conversion of mass (positron and electron) into energy (photons). According to the principle of conservation of energy, it will be:

$$E_\gamma = h \cdot v = 2m_e c^2 + E_e^- + E_e^+ + E_M \ , \tag{1.5}$$

where E_e^- , E_e^+ and E_M are the kinetic energies of the electron, the positron and the daughter nucleus. Ways photons interact with matter are the photoelectric effect, the Compton scattering and the pair production [2].

1.1.4 Detectors and Electronics

The PET system includes a detection device, an electronic system, a coincidence processor, data acquisition, storage and image reconstruction.

PET imaging aims to calculate the activity of the radiopharmaceutical contained in each tissue voxel. If two photons are detected simultaneously in detectors that are located opposite to each other, an annihilation event occurs in at some point on the line connecting the two point's incidence. The line connecting the two detectors is called Line of Response (LOR). This records the activity of the radiopharmaceutical in the tissues. After the detection of several (some 100k) annihilation events, the distribution of the positron-emitting radiopharmaceutical is calculated by special mathematical reconstruction algorithms [1, 3].

1.1.5 Detection set up

The detection array of gamma rays consists of a 360^o ring in which multiple detectors are arranged in groups (blocks). The crystals of the detector are lined up next to each other in a circle shape. The main crystals used in PET are BGO, LSO, GSO, and LYSO. Within the context of the thesis at Biomedical Research Foundation (BRFAA) of the Academy of Athens, the study was conducted using the SIEMENS Biograph Vision PET/CT scanner. Detectors consist of three parts: 1) Scintillators, 2) Diodes, 3) Electronics [1, 3].

1.1.6 Scintillators

Inorganic crystalline scintillators are used, in which the excitation of their atoms results in the production of light. The photons passing through the crystal produce free electrons and holes, the electrons wander until they are trapped by an activated center. Afterwards, the e^- is excited and then de-excited by emitting light in a wide spectrum in the visible region. The photons interact with the crystal through the photoelectric effect or Compton scattering. Specific illuminators transport the light through a specific patch, then is converted into a short electrical impulse. The size of the impulse will be proportional on average to the energy deposited by the detected annihilation photon in the crystal block.

The crystals must have the following characteristics:

- Small with good spatial resolution,(high Z and density).
- High absorption capacity (high sensitivity in 511 keV gamma detection).
- Small decay time (reduction of accidental prompt events and time-Of-flight).
- Important light output (energy resolution and crystal transparency).

	BGO	**GSO**	**LSO**	**LYSO**
μ (cm^{-1})	0.95	0.67	0.85	0.8
Density (g/cm^3)	7.13	6.71	7.4	5.4
Energy resolution	40%	28%	35%	35%
Light output (Photons/MeV)	8200	10000	28000	34000
Decay time (ns)	300	60	40	40

Table 1.1: Scintillators in PET imaging

Each pair of detectors in the ring defines a possible emission path. Over the course of a PET scan, the system is counting how many times each pair of detectors is hit in coincidence. For a ring with n detectors, there are $n^2/2$ ways to pair up the detectors, so a great deal of information is recorded [3].

The SIEMENS Biograph Vision PET/CT scanner uses 3.2 mm LSO crystals for the detector. This scintillators exhibit superior features for faster time-of-flight and better image quality, which implies to higher light output and faster scintillation [4].

Biograph PET/CT scanner	TOF performance	TOF Gain3
Biograph Vision	214ps	6.2

1.1.7 Optiso Ultra Dynamic Range (UDR) detector

The detectors employed by the Siemens Biograph Vision PET/CT scanner are the Optiso UDR's detectors. These detectord use smaller crystal elements and block size which improves detectability by delivering 60% better volumetric resolution. According to the manufacturer, the 3.2-mm LSO crystals move silicon photomultiplier (SiPM) technology to more precise imaging with detection of small lesions, devise accurate treatment strategies, and optimal performance in a wide range of count rates. The technology feature of SiPM is about the performance of time-of-flight, which depends on capturing light emitted by all photons during scintillation. The Optiso UDR detector is crafted to ensure that Silicon Photomultipliers (SiPMs) span the entire LSO-array surface, capturing all light emitted during scintillation. This results in full coverage and facilitates swift temporal resolution.

Fast time of flight and high effective sensitivity provide good results in low and medium activity ranges such a ^{68}Ga, ^{18}F and ^{90}Y applications. The small block detectors with low dead time makes it suitable to handle high concentrations of activity, particularly in studies involving tracers with very short half-lives, such as ^{82}Rb and ^{15}O.

The ultra-fast time-of-flight improve signal to noise ratio enabling faster scans, lower injected dose and better image quality. Also, increases detectability of small lesions and allows the creation of smaller sections along the Line of Response, enhancing the precision in pinpointing the location of the annihilation event [5].

1.1.8 Time-of-Flight

Time-of-Flight (TOF) technology minimizes the spread of noise along the lines of response by measuring the detected time difference of the two 511 keV gamma rays. Noise reduction is comparable to enhancing the Signal-to-Noise Ratio (SNR), Noise Equivalent Count (NEC), and sensitivity allowing a decrease in radiation dosage and/or scanning duration [1, 2, 3].

The equation that describes TOF-SNR is:

$$TOF_{SNR} = \sqrt{\frac{D}{c \cdot \Delta t}},$$

where D the object size, c is the speed of light, and Δt is the timing resolution.

Therefore, faster timing resolution is required when object size is smaller. Due to the "Poison nature" of PET data, this translates into a sensitivity gain of

$$\frac{D}{\Delta x} \implies \frac{D}{1.6\Delta x},$$

under the condition that Δx is greater than or equal to twice the detector spatial resolution. The factor that affects the TOF imaging performance of a PET scanner is the system coincidence timing resolution that is determined by the choice of scintillator, photo-sensor and the detector design [6]. In addition, the Optiso UDR detector with 3.2 mm LSO crystals has the ability for best timing performance using custom electronics that are stable and perform well at high count-rates. For the specific system employed the TOF is equal to 214 ps [5].

1.1.9 Processor- Coincidence detection: True, Scatter and Random events

Annihilation Coincidence Detection (A.C.D.) . In addition to true coincidence events, which occur when photons from the same annihilation event are detected without scattering in the patient or bed, there are other types of coincidence events. They originate from scattering or from random photon coincidence due to different annihilation effects, which result in the false assignment of the LOR. This set of LORs is a projection view of the radioactivity distribution in the body in that slice.

The coincidence circuit is used in order to detect and identify the photons originating from electron-positron annihilation. Initially, a pulse from the detector is directed to the constant fraction discriminator (CFD), which generates a square pulse with a defined width and height. The requirement is for the height of the analog pulse, which describes the photon's energy, to be above a specified minimum threshold. To have a coincidence, two signals must have a time difference smaller than a given time interval T, which is referred to as the coincidence time window

(T=10 ns). This time window must be large enough so that all true annihilation events are included, since the photons may have a time difference in their time of flight. However, it must be kept within a specific finite range to avoid recording random events.

Random counts add background to the image. Random events become significant (compared with true events) when detector rates are very high, and are more problematic for detectors with low detection efficiency for three-dimensional imaging. There is also a time delay from the photon detector, which depends on the emission time of the scintillators and whether the electrons used are fast enough,

$$T = T_{\text{det}} + \frac{\rho}{c}.$$

By reducing the time delay of the detector, we decrease the number of random coincidences and allow the measurement of the TOF of photons from the point of the annihilation site to their detection in TOF-PET systems.

Regarding the coincidence processing, pairs of coincident photons, or events, detected are stored in matrices (tables) or sinograms, where each row in the matrix represents a parallel projection p(s, φ) of the distribution of the radiopharmaceutical activity in the patient at a specific angle (φ) and position (z). The sinogram is represented as the distance across the field of view of the scanner plotted against the angle from which the projection is taken.

When one or both photons Compton scatter in the object (patient) they form a scatter coincidence. Therefore, the event we have in PET is precisely defined on the line connecting the two detectors LOR and results the loss of events from their original LOR. Compton scatter causes a loss of contrast in imaging systems and can be partially removed by energy discrimination [1, 3].

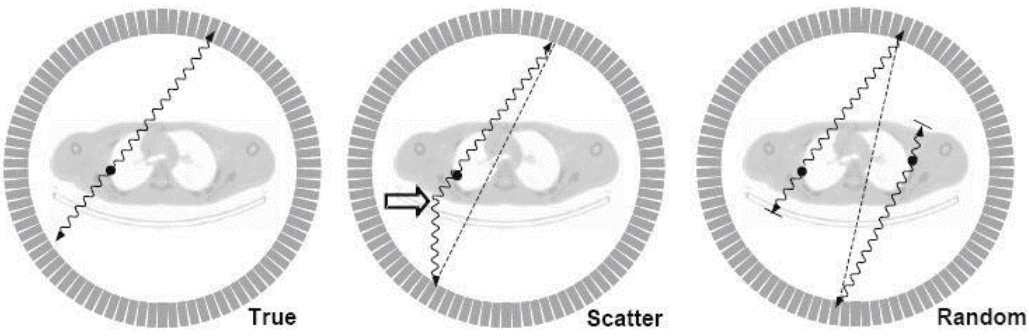

Figure 1.3: Three types of coincidences in a PET detector, Source: ResearchGate.net

Additionally, there is a possibility that one of the two photons may lose all of its energy, rendering it undetectable. In such cases, attenuation occurs. The attenuation is independent of the annihilation position and, consequently, the line of response. Thus, an external source is used to measure and correct the attenuation.

Data correction

When trying to measure or analyze images, various adjustments and corrections are applied to enhance the accuracy of the results. These corrections include factors like reducing the impact of signal weakening, accounting for random events, addressing scattered signals, compensating for delays in measurement, standardizing measurements, accounting for background noise, considering the natural decay of radioactive materials, and adjusting for sensitivity differences [3].

Random's

A pair of annihilation photons striking two detectors at the same time is termed a true count or true coincidence annihilation event. When two atoms decay at nearly the same time, photons from two different annihilation events may be detected within the timing window. When this happens, a false event referred to as a random event, is recorded and its false LOR is shown as a dotted line on Figure 1.3. Many atoms are decaying at nearly the same time, random events cannot be avoided. Processing software estimates these false events and applies corrections during reconstruction [1, 3].

To obtain quantitative data in PET it is necessary to estimate and subtract the random coincidences from the measured data in each LOR to yield the sum of the true and scattered coincidences. The rate of random events on a particular LOR between two detectors is given by:

$$R_R = 2\tau \cdot R_1 \cdot R_2, \tag{1.6}$$

where R_1 and R_2 are the rate of random events for detector 1 and detector 2, respectivelly, and τ is the time window. Random counts add background to the image. Random count rates are also higher when there is more activity present or

when the scanner is on 3D mode. At the presence of a radioactive source just outside the scanner's field-of-view (FOV), the random events may be 50% of all coincidence events detected. Random coincidences decrease image contrast. Thus, hot lesions and tumors may be missed [1, 3, 7].

Scatter

Another miss-positioning error of PET data originates from the scatter of annihilation photons between their origin and the detectors. The degree to which scatter events are accepted depends on the energy resolutions of detectors and the associated lower energy threshold of the energy window. Scatter is affected by the distribution of radioactivity, size, and density of the object and their location relative to the detectors.

Approximately, 50% of photons scatter within the body. Therefore scatter correction and accurate attenuation correction are necessary when quantitative information is needed. The solution for most scatter is to use shields that block radiation originating outside the field of view (FOV) of the ring. Flat, ring-shaped lead or tungsten septa are used, not only to reduce the number of scattered events collected, but also to minimize other effects of radiation originating outside the FOV, including dead-time and random events. Scattered photons have less energy than unscattered ones, but total discrimination based on energy is not possible because some unscattered photons deposit only a portion of their energy in the detectors. Scatter events are approximately 15-50% of all coincidence events detected.

Therefore, several post acquisition scatter correction methods have been suggested, including the dual energy window approach, model-based scatter correction and Monte Carlo simulations. The methods in widest use to date are the "Gaussian fit" technique [8], and model-based scatter correction algorithms [9]. The Gaussian fit method consists of fitting a Gaussian profile to the scatter tails found at the edge of each projection. This works well in brain scanning, where the activity and the scattering medium is fairly uniformly distributed and concentrated in the center of the field of view, resulting in a simple slowly changing scatter distribution.

The model-based scatter correction algorithms use the attenuation map obtained from a transmission scan together with the emission data and a model of the scanner geometry and detector systems to calculate the percentage of photons falling on

each detector, using the Klein-Nishina formula. The Klein-Nishina formula gives the differential scattering cross-section as a function of the scattering angle [1, 3].

Dead time

The conversion of gamma ray energy into an electronic pulse and the processing of the pulse requires a finite amount of time that is often referred to a dead time. If events happen too rapidly, they cannot be properly analyzed and information is lost. As the rate of photons hitting a detector increases, the probability of missing a photon due to detector's dead time increases. This problem is particularly troublesome for coincidence detection, because both photons must be detected. Dead time losses are minimized by systems with many independent detectors. Losses are also reduced by faster scintillators and processing electronics. This is usually done by modelling the dead-time losses as a combination of paralyzable and non-paralyzable components and obtaining parameters for the model by means of experiments involving repeated measurements of a decaying source [1, 3, 10].

1.1.10 Noise

Reducing image noise, which refers to random variations in pixel intensity, is a critical aspect of nuclear medicine imaging. Increasing the number of counts can effectively minimize noise. Achieving more counts can be accomplished by extending the scanning duration, increasing the dose of the radiotracer injection, or optimizing the scanner's ability to detect emitted radiation. An important factor in the noise quality of data is the level of background.

During a PET scan, the counts measured along a specific line of response include various types of events: true, random, and scattered. The total counts measured throughout the scan are represented as P. True events are calculated by subtracting the sum of random and scattered events from the prompts. However, relying solely on the number of true events (T after correction) as an indicator of subsequent image quality is insufficient [1, 3].

1.1.11 Spatial resolution

Spatial resolution is an important factor in PET image quality. Characterizes the system's ability to resolve spatially separated sources of radioactivity.

The smaller the crystal element or the more finely sampled the detector, the better an event can be localized and the better the spatial resolution will be. If a crystal has a low density and low atomic number Z, γ rays will travel further before interacting, compared with a high density, high Z material. The ability to stop γ rays is referred to as the material's stopping power; detectors with higher stopping powers will have more accurate spatial localization than those with low stopping power because there is less inter-crystal scatter.

Spatial resolution is also affected by the energy of the photon and, for scintillation detectors, the efficiency of collection of the scintillation light. The energy of the γ ray that is deposited in the crystal determines the amplitude of the measured signal, which in turn defines how accurately it can be localized in the detector:

- The positron emission point differs from its annihilation point, due to mean kinetic energy of the positron. Range= 0.2-3 mm.
- The gamma ray from annihilation: $\phi \neq 180^\circ$ and $E_{\gamma 1} \neq E_{\gamma 2} \neq 511\,\text{keV}$. In reality $\phi \neq 180^\circ \pm 0.25^\circ$ and $E_\gamma = 511 \pm 40\text{keV}$, non-collinearity due to non-zero kinetic energy of the positron during the annihilation.
- Detector size.

The spatial resolution of the PET scanner images is typically 4-5 mm, and the CT images is 1 mm. However, it is noteworthy that in Nuclear Medicine Department of BRFAA,the Siemens Biograph Vision-450 PET/CT has 3.2 mm LSO crystals, indicating increased resolution compared to standard PET scanners [3, 11].

1.1.12 Detector normalization

The sensitivity of a particular LOR is strongly affected by the angle that the LOR makes with the two detector faces at each end. This means that the sensitivity of the LOR relative to the mean is affected both by the geometry of the camera and the LOR position. Apart from such geometric effects, the block detectors themselves

vary in efficiency, as the scintillation crystals are not all identical. In order to avoid image artefacts and have an exact quantification correction through a process, is necessary.

The process of correcting for these effects is referred to as normalization, and the individual correction factors for each LOR are referred to as normalization coefficients (NCs). The problem can be overcome by using a component based variance reduction method (e.g. Hoffman et a1 1989) [12]. NCs are modelled as the product of intrinsic crystal efficiencies and a small number of geometric factors that account, for example, for the variation in crystal efficiency with photon incidence angle. There is a trade-off between systematic errors and statistical accuracy that depends on the complexity of the model [7, 13].

1.2 Radioactive Decay

Some nuclei are radioactive and decay into daughter nuclei while simultaneously emitting radiation in the form of particles or photons. The quantity that quantitatively characterizes the radioactivity of an element is its activity, defined as the number of nuclei that decay in a unit of time (e.g., per second). The activity is measured in MBq (megabecquerels) or mCi (millicuries), with the relationship 1 mCi = 37 MBq. The number of radioactive nuclei decreases over time as they decay and transform into their daughter nuclei. The law that governs this decrease in the number of nuclei or, equivalently, the activity of an element, is described by the following equation:

$$N = N_0 e^{-\lambda t}, \tag{1.7}$$

where N is the current number of radioactive nuclei (activity) at a given time, λ (lambda) is the decay constant, a unique property of each radioactive element. When N decreases to half of its initial value, this is known as the half-life. The half-life is the time it takes for half of the radioactive nuclei to decay [3].

1.2.1 Effective Dose

The probability of stochastic outcomes arises not only from the equivalent dose but also from the irradiated tissue or organ. For an equal dose to the pituitary and adrenals, the probability of cancer incidence differs. The factor that weights the equivalent dose is called the tissue weighting factor (w_T). The values of w_T are chosen so that a homogeneous equivalent dose throughout the body attributes to an effective dose numerically equal to that homogeneous equivalent dose. In this case, the sum of the double-weighted absorbed doses, both for radiation quality and irradiated tissue, is called the effective dose, E.

In each case, radiation refers to either that originating from a source outside the body or from a source within the body, namely, radioactive material. The effective dose is also measured in Sievert and is related to the whole-body dose, given by the equation:

$$E = \sum_T w_T \cdot H_T \rightarrow E \sum_T w_T \cdot w_R \cdot D \ , \tag{1.8}$$

where w_R is the weighting factor which depends on the type of radiation, and $D = E/m$ is the absorbed dose of the tissue or organ [14]. Please note that $w_R = 1$, for x-rays and γ-rays.

Tissue-organ	$\mathbf{w_T}$
Bone marrow, lungs, stomach, ***adrenal glands***, extra thoracic region, breast, gallbladder, heart, kidneys, lymph glands, muscles, mouth epithelium, pancreas, prostate, small intestine, spleen, thymus gland, uterus/cervix	**0.12**
Gonads	0.08
Bladder, esophagus, liver, thyroid	0.04
Bone surface, ***brain***, salivary glands, skin	**0.01**

Table 1.2: Weighting coefficients of the exposed tissue w_T for the calculation of the effective dose E_{eff} [15, 16].

1.2.2 Sensitivity

System Volume Sensitivity (SVS) is a metric used in imaging to assess the performance and sensitivity of the imaging system. It quantifies the ability of the PET/CT scanner to detect and accurately measure radioactive signals emitted by a radiotracer within a specific volume of interest. In essence, it tells us how well the scanner can capture and measure the activity within a given region. The sensitivity correction is calculated by imaging a uniform phantom with a known radioactivity concentration of comparable size to the objects likely to be imaged.

$$SVS = \frac{\text{Activity in ROI}}{\text{Total injected Activity}} = \frac{\text{counts/sec}}{\text{MBq/voxel}} \rightarrow SVS_{\text{normalized}} = \frac{SVS}{\text{Volume of ROI}} \,. \tag{1.9}$$

From the performance measurements of NEMA NU-2 2018 report, the effective sensitivity of SIEMENS Biograph Vision-450 SiPM based digital PET/CT system, is calculated and confirmed as 100cps/kBq [17, 18].

1.2.3 Calibration

Correction calibrations are those that compensate for the inherent variations in the scanner and perform meaningful scaling on the image, such as normalization, blank scan, and absolute activity calibrations. *Blank scans* are performed daily to provide accurate transmission scan data for attenuation correction of images. Radioactive decay of the transmission sources, dead time corrections, and detector sensitivity may vary frequently. The blank scan, however, is data that represent the sensitivity response to the transmission source without any attenuating material (or patient) being present in the gantry ring.

Normalization calibrations are done to measure the efficiency for all LORs. Also, are performed by rotating radioactive rod sources, which contain a low activity source of radioactivity, and acquiring data that will be used to balance the efficiency of all detectors in the scanner. It is performed at low count rates to simulate the count rate of patient data and approximate the level of dead time losses seen during patient acquisition.

Absolute Activity Calibration factors are used to convert pixel values into a measure of absolute activity per voxel. This calibration is performed by taking a precisely

known amount of activity and loading a water filled phantom whose volume is accurately known. The phantom is imaged, reconstructed and processed into a set of correction factors that allows the conversion of a patient scan into a presentation of percentage of injected dose per volume or gram of tissue. This calibration process ensures that the PET images accurately represent the distribution and concentration of the radio-tracer within the body. This technique not only enhances the accuracy of quantitative measurements but also provides a quantitative image to measure the standard uptake values ($SUVs$) of tissues or tumors [19, 20].

1.3 PET and PET/CT Imaging Phantoms

1.3.1 Physical Phantoms

In medical imaging, physical phantoms refer to real objects designed to simulate the human body, or parts of it, for specific clinical conditions. Physical phantoms are used to calibrate imaging systems, to evaluate their performance and to ensure the correct operation of imaging systems before scanning human subjects. They also constitute an inexpensive way of testing new imaging applications and serve as a well-defined reference for quantitative measurements.

In oncology, four principal tomographic imaging modalities are used in clinical routine for the diagnosis and characterization of malignancies. Two of them are, the Positron Emission Tomography (PET) and the Computed Tomography (CT). Therefore, specific phantoms exist for hybrid imaging systems such as PET/CT and PET/MRI, serving specific needs of each imaging component. The combined imaging modalities provide complementary morphological and physiological information within a single examination, thus, improving diagnostic accuracy and subsequently patient management. Since tumor characterization is critical for the diagnosis/grading, treatment planning, and follow-up of the oncological patients, different methods aim to quantify the characteristics of the tumor (i.e. length, volume, SUV).

The principle of PET imaging is the detection of gamma rays (511 keV) originating from the annihilation of positrons with electrons within the examined object. Positron emitters with short half-life such as ^{68}Ga are labelled to specific biological molecules and injected into the patients. Depending on the carrier molecule, the radioisotope is distributed across different body tissues, providing physiological

information from the region of interest.

Therefore, a critical requirement for the design of PET imaging phantoms is the feasibility to simulate radiotracer activity distributions similar to those expected in clinical PET studies. The compartment materials, should also have low photon attenuation coefficients and be as similar as possible to the human body tissues. The main phantom concept is to simulate heterogeneous tumors - like radioactivity distributions consisting of cylindrical containers. This technique is performed with quantities of silica gel molecular sieves placed in four cylindrical probes to create heterogeneous regions with different spatial radioactivity distributions [3, 21, 22].

1.3.2 Calibration Factor

Calibration factor is a critical parameter that relates the detected signal to the actual concentration of the radio-pharmaceutical. It allows the conversion of the signal intensity into activity and is measured in MBq/count. It is defined experimentally using a cylindrical phantom. CF is defined as the ratio of the known activity in the phantom to the signal intensity in the ROI and is calculated as follows:

$$CF = \frac{A}{V} \times \frac{P}{C} = \frac{\text{Known Activity in the phantom}}{\text{Signal Intensity in the ROI}}, \tag{1.10}$$

where A/V is the known activity concentration in the phantom [Bq/mL], P is the positron fraction; for ^{68}Ga the probability of positron emission is equal to 89%, and C is the average voxel value expressed in arbitrary units of PET images [counts/voxel/sec] [19, 20].

1.3.3 Quantitative image information

The absolute quantitative uptake of the radiotracer in tumors can be measured in an effort to differentiate between malignant and benign tissue. The SUV is useful in measuring tumor metabolic function. PET scanners allows the conversion of image data into an activity measured of radiotracer uptake per pixel or voxel in the image. Standard uptake value measurements are based on the injected activity per patient weight in kilograms. The injected activity (minus residual in the syringe) must be accurately known and the time of injection recorded. Tumor SUV is determined by placing a Region of Interest (ROI) over the tumor and using computer programs to

calculate the value.

$$SUV = \frac{\text{ROI activity concentration (MBq/ml)}}{\text{Injected Activity (MBq)}} \times \text{body weight (g)} \ . \tag{1.11}$$

SUV changes with time, so it is critical to specify the time at which the SUV image was obtained. The value becomes unitless if it is assumed that 1 g of body weight is equal to 1 mL. The higher the number of SUV, the more probable it is that the given lesion is malignant. Usually in patients with Gastroenteropancreatic-Neuroendocrine Tumors (GEP - NETs), if the SUV exceeds the maximum SUV of the spleen, it suggests a suspicious finding.

Thus, the SUV indices from ^{18}F-FDG PET/CT imaging hold significant prognostic and predictive value which is helpful in monitoring cancer response to therapy in individual patients. However, the assessment becomes more complicated with ^{68}Ga-DOTA-peptide PET/CT scans due to distinct mechanism of action. Unlike FDG, which tracks glucose metabolism, ^{68}Ga-DOTA-peptide PET/CT evaluates the expression of somatostatin receptors. High levels of SSTR2 expression could predict a beneficial response to treatment. However, during the patient's follow-up, SUV measurements may continue to remain high. This does not necessarily indicate treatment ineffectiveness, but rather necessitates further evaluation of the tumor biology. Conversely, the opposite scenario may also occur [23, 24].

1.3.4 Recovery coefficient

Recovery Coefficient is intended to correct the radiopharmaceutical uptake values that are influenced by factors such as Partial Volume Effect (PVE), dead time, scatter, attenuation, activity distribution etc. RC was estimated as suggested by the NEMA and IEC standard using the equation below. The various parameters of the equation where determined by drawing different ROIs within each of the spherical hot spot and background areas.

$$RC = \frac{AC_L - AC_{BG}}{AC_C - AC_{C_{BG}}} \ . \tag{1.12}$$

RC refers to the recovery concentration for a region of interest (ROI). AC_L denotes the radiopharmaceutical activity concentration measured in the ROI. AC_{BG}

represents the radiopharmaceutical activity concentration measured in the ROI of the background. AC_C indicates the radiopharmaceutical activity concentration that was previously known and inserted in the ROI. $AC_{C_{BG}}$ signifies the radiopharmaceutical activity concentration that was previously known and inserted in the ROI of the background. All radiopharmaceutical concentrations are expressed in units of Bq/mL.

For our analysis of PET phantoms, we report results as the dimensionless recovery coefficient RC, defined as the ratio of the measured values to the known value and is calculated as follows:

$$RC = \frac{A_M}{A_K}, \tag{1.13}$$

where AM is measured radioactivity concentration (kBq/mL), averaged over voxels in the ROI, and AK is the known NIST implicitly traceable concentration [1, 4].

1.3.5 Pharmacokinetics - Kinetic modelling

Reubi's investigation into the SSTR subtype affinity profile of several somatostatin analogs revealed that DOTA-TOC possesses a notable affinity for human SSTR2. Consequently, ^{68}Ga-DOTATOC binds effectively to cells exhibiting an upregulation of SSTR2, including malignant cells. The intensity of PET/CT scan signals varies depending on the distribution and concentration of somatostatin receptors (SSTR) within the tissue. The increased presence and density of receptors leads to higher uptake of the radioactive tracer, thus producing more intense signals in PET scan images [25].

This complex interaction between receptor affinity and tracer distribution underscores the importance of understanding the pharmacokinetics of ^{68}Ga-DOTATOC, a radiolabeled somatostatin analog, particularly in the context of nuclear medicine imaging for GEP-NETs. Upon intravenous administration, ^{68}Ga-DOTATOC quickly disperses throughout the body due to its high lipophilicity and robust affinity for somatostatin receptors (SSTRs) expressed on various tissues, notably NETs. The precise evaluation of how ^{68}Ga-DOTATOC interacts with GEP-NETs relied on a kinetic model comprising two tissue compartments and an extra compartment for blood. There are only a few studies in the literature that have investigated the speed

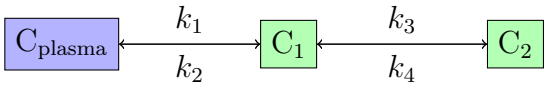

Figure 1.4: Compartmental configuration for kinetic model.

at which ^{68}Ga-DOTATOC moves within tumors.

A model featuring two compartments for tissues and an additional one for blood was employed to assess the rate constants (k_1, k_2, k_3, k_4, and V_b). This model is suitable for investigating receptors, as noted in the study by Henze et al., and its specifics were elucidated by Burger and Buck. In Fig. 1.4 C_1 represents the tracer specifically bound to tissue, while C_2 signifies the tracer's internalization into cells. For substances active on receptors, such as ^{68}Ga-DOTATOC, k_1 relates to receptor binding, k_2 to detachment from the receptor, k_3 to cellular uptake, and k_4 to release from cells. Each parameter (k_1–k_4) was considered acceptable when it was below 1. The fractional blood volume (V_b), associated with blood volume interacting with tissue, was separately determined using the Marquard algorithm, an iterative method for optimizing parameter configurations [26].

The compartmental kinetic model describes how a tracer behaves in the body over time. It helps create a mathematical function that shows the tracer's activity (TAC), based on factors like how quickly it binds to tissues, how much stays in the blood vessels, and its concentration in the blood. This function can be matched with real-time data from dynamic scans to find out how fast the tracer moves in and out of tissues.

Graphical methods simplify this data to show linear patterns after a certain time, revealing important rates like influx rate (K_i) and total distribution volume (V_T). V_T is often used in studies to understand receptor availability or calculate specific measures like distribution volume ratio (DVR) and binding potential (BP). K_i is a biological index that is used to grade neuroendocrine tumors (NETs) based on their rate of cellular proliferation.

1.3.6 Radiopharmaceuticals

Radiopharmaceuticals are pharmaceutical products that contain radioactive isotopes, which are safe for administration in diagnostic or therapeutic applications. They are distinguished primarily by their characteristics, including a relatively short

half-life, radiation energy, and the ability to selectively penetrate the tissue for which they are designed, both at the initiation and during the reaction. In PET radiopharmaceutical is composed of a biologically active pharmacophore and a positron-emitting radionuclide, and belongs to a unique species in pharmaceutical field. The most common radionuclides for PET radiopharmaceuticals include ^{11}C, ^{15}O, ^{13}N, ^{18}F, ^{68}Ga and ^{82}Rb [27].

Radionuclide	$\mathbf{T_{1/2}}$	**Ci/μmol**	$\beta^+(\%)$	**Max** E_β**(MeV)**	**Max** β^+ **range(mm)**	**Production**
^{11}C	20 min	9220	99	0.96	4.1	Cyclotron
^{15}O	123 sec	90,800	100	1.19	5.1	Cyclotron
^{13}N	10 min	18,900	100	1.72	7.3	Cyclotron
^{18}F	110 min	1710	97	0.635	2.4	Cyclotron
^{68}Ga	68 min	2766	88	1.9	8.2	Generator
^{82}Rb	78 sec	150,400	95	3.35	14.1	Generator

Table 1.3: Characteristics of common positron emitters.

Where, $T_{1/2}$ is the half- life and $Ci/\mu mol$ is the max specific activity. The diagnostic radioisotopes are based on the penetrating property of electromagnetic radiation which is detected externally. Therefore, the radionuclide should meet certain requirements:

- Photon or positron emission.
- Short half-life to reduce the overall exposure of the patient, but sufficient enough to achieve the composition and the illustration.
- The half-life of the radioisotope should match the biological half-life of the radiopharmaceutical.
- The energy must be detectable and not absorbed by the tissues.
- Easy to prepare, with low cost and high availability. Thus, generators are preferred.

Then, the appropriate chemical compound is labelled with the radioisotope, resulting in the production of the radiopharmaceutical. The chemical and biological purity of the radiopharmaceutical is also checked, which prevents toxic radiocontamination of the patient.

Regarding the decay mechanism, the inherent advantage of positron-emitting radionuclides compared to gamma-emitting ones is closely tied to the advantages of PET technology. These include enhanced sensitivity, resolution, quantification capabilities, and the ability to conduct dynamic scans. In particular, the superiority of ^{68}Ga-DOTATOC PET-CT over ^{99m}Tc-MDP SPECT and ^{111}In-DTPA-octreotide SPECT, is attributed not only to the fundamental advantages of the technology but also to the analogous coordination chemistry observed in ^{68}Ga, ^{90}Y, and ^{177}Lu, which enables the possibility of using the same molecule as a carrier for subsequent radiotherapy [25, 28].

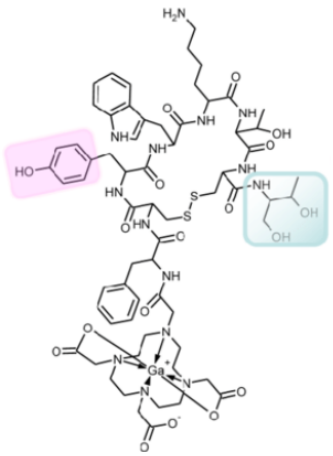

Figure 1.5: ^{68}Ga-DOTATOC, Source:ResearchGate.net

Overall, the figure seems to represent the chemical structures of two molecules: one in the pink rectangle and the other in the blue rectangle. The molecule in the pink rectangle appears to be a peptide-based compound (DOTA-TOC), characterized by its chain-like structure composed of amino acids linked together. Peptides are organic compounds consisting of multiple amino acid residues bonded together by peptide bonds. The molecule in the blue rectangle appears to be a complex involving gallium (Ga). It is a chelating agent or ligand that forms a complex with gallium ions.

1.4 CT - Computed Tomography

Computed tomography (CT) is an imaging method of the body based on the absorption of x-rays by body tissues. When x-rays pass through a material, a portion of the radiation is absorbed by it. The amount of x-ray absorption depends on the nature of the material, the wavelength of the x-ray, and the thickness of the material.

Computed Tomography is based on the mathematical reconstruction and visualization of the internal structure of a body after processing data from multiple projections. Thus, two-dimensional objects, such as the cross-sections of the human body, can be reconstructed from one-dimensional projections in multiple directions onto the plane of each section. Subsequently, three-dimensional objects can be reconstructed from their multiple two-dimensional projections by the internal integration of similar tissues in successive sections [29].

The basic components that constitute a Computed Tomography system are:

- The generator
- Gantry
  - x-ray Source (x-ray tube)
  - Detectors
  - Shielding elements
- Data Acquisition System (DAS)
- Image Reconstruction
- Patient table

1.4.1 Generator

The generator functions by supplying the required electrical power to produce x-rays, utilizing two distinct types of electrical currents. One type is a high voltage, typically ranging from 20 to 150 kilovolts, which sets the upper limit for the intensity of the x-rays generated. By increasing this voltage, the electrical potential difference between the anode and cathode is heightened, consequently enhancing the x-ray production.

On the other hand, there's a separate, fixed low voltage supply, approximately 10 kiloVolts, specifically directed to the cathode filament. This low voltage supply facilitates a continuous emission of electrons through a thermionic reaction. In simpler terms, it ensures a steady release of electrons required for the x-ray production process [29].

1.4.2 Gantry- Scanning Unit

A scanning unit, also known as a gantry, is the structure that contains the x-ray tube, shielding elements, and photon detectors. Positioned facing each other, the x-ray tube and photon detectors are designed to rotate seamlessly in one direction around the patient, completing a full 360-degree rotation. Gantry tilt refers to the angle formed between the plane of the x-ray tube and the vertical plane. In modern CT machines, gantry tilt typically ranges between -25 degrees and +25 degrees. This angle can be adjusted by the CT operator based on the specific objectives of the examination, such as minimizing image artifacts or enhancing the healthcare provider's ability to perform an invasive CT-guided procedure. The use of slip rings in gantries allows continuous and unrestricted circular movements of internal components without the risk of cables or circuits becoming tangled. Moreover, the gantry includes ample space to accommodate both the patient and the table, facilitating their passage through the system during scanning procedures [29].

1.4.3 X-ray Tube

In the tube, electrons are produced and accelerated, which then hit the anode of the tube, emitting x-rays. The lamp has a rotating anode and a very small anode focus. The typical operating voltage of the lamp in our CT scanner is 80 to 100 kV and does not vary significantly during the different types of tests. The value of the anode current of the lamp, measured in mA when multiplied by the time of the lamp, measured in seconds, gives a characteristic physical quantity which called mAs. Its value varies from test to test [29].

1.4.4 Detector system

The photon detector plays a crucial role in capturing and quantifying the photons emitted by the x-ray tube as they pass through the patient's body. This detector comprises two essential layers: the scintillator layer and the photon tide layer. The scintillator layer serves to convert the x-ray photons absorbed by the detector into visible light photons. Essentially, it transforms the high-energy x-ray photons into a form of light that can be detected and processed. Following this conversion, the photon tide layer comes into play. Its role is to further convert the visible light photons into electrical signals. This conversion process allows for the translation of the detected light into electrical data that can be analyzed and interpreted by the imaging system [29].

1.5 CT Imaging

The feature of Computed Tomography that gives it significant capabilities in medical diagnosis is its high sensitivity to small variations in the attenuation coefficient (or optical density) μ, of the soft tissues of the human body. Thus, instead of the soft tissue appearing uniform, as is the case in plain radiography, CT can distinguish between fat and protein. The sensitivity of CT to variation in μ is on the order of 0.5% which is sufficient for distinguishing between fat and protein. In practice, each section of human anatomy is depicted on a regular square grid $m \times n$ values of the attenuation coefficient $\mu_{m\times n}$.

Suppose, for a given direction of the x-ray beam through the body, this direction coincides with the first row of the square grid, namely with pixels μ_{11} and μ_{1n}. Before passing through the body, x-ray beam has a predetermined and known intensity Io. It then passes through the body and undergoes attenuation due to absorption and scattering effects, resulting in the intensity I, which is significantly reduced and recorded by the corresponding detector.

The intensity of the beam in the specific direction, as described above is given by the relation:

$$I = I_0 e^{-(\mu_{11}+\mu_{12}+\mu_{13}+\cdots+\mu_{1n})\Delta\chi} \tag{1.14}$$

Where μ_{11}, $\mu_{12}\ldots$ μ_{1n} are the attenuation coefficients of voxels of tissues en-

countered by the x-ray beam on its path, passing through the first row of the m×n grid. $\Delta\chi$ is the distance travelled by the beam within each elemental volume of tissues. When the beam passes through the second row of the grid, the corresponding values of the attenuation coefficient included in the equation are μ_{21}, μ_{22}, ..., μ_{2n}. In this way, the elemental volumes of all points of the grid are scanned, i.e., all the elemental volumes of the body section.

Effectively, the value of $\Delta\chi$ has been chosen in advance by the manufacturer of the CT system and determines the spatial resolution which is of the order of 1 mm. It is possible for the same system to operate with more $\Delta\chi$ values, depending on the operator's choice, thus enabling reconstruction of anatomical images at higher magnification.

Specifically, the source of x-rays generates a diverging beam, which has a fan-shaped form. The rays of the beam penetrate the human body, and when they exit from the other side of the body, they are detected by a circular array of detectors. Each detector measures the absorption of a thin beam that passes through a different line/region of the body, which is represented by a corresponding line of pixels of the aforementioned grid $\mu_{m\times n}$.

The x-ray source rotates around the human body, and the computer processes information from thousands of absorption data. Through parallel data collection, the time required for scanning each section is short. With this technique, volumes or other abnormalities can be detected, as the pixels corresponding to any volumes or abnormalities have values $\mu_{m\times n}$ somewhat different from those of the surrounding tissues. Additionally, it is possible to distinguish between adipose and muscular tissue, which is very important for applying the method to body composition measurement [30].

1.6 Dose

1.6.1 Absorbed dose

In radiation protection it is mainly used in the term average absorbed dose to tissues or organs, i.e. as the ratio of the mean energy imparted $d\bar{\varepsilon}$ to matter of mass dm by ionising radiation.

$$D = d\bar{\varepsilon}/dm \ . \tag{1.15}$$

Energy is measured in *Joules* and mass in kg. From the equation it follows that the unit of measurement of absorbed dose is $Joule/kg$. For convenience, we denote this unit as Gy (gray). The gray is a relatively large unit, so smaller sub-multiples such as milligray (mGy) or micro-gray (μGy) are often used in practise [1].

1.6.2 Equivalent dose

In order to take into account the biological impact caused by radiation on a tissue, the concept of equivalent dose is used. The equivalent dose (H_T) received by a tissue, T, is derived from the multiplication of the absorbed dose (D) by a weighting factor (W_R), which depends on the type of radiation.

$$W_T = D \times W_R \ . \tag{1.16}$$

The unit of measurement of the Equivalent dose is the Sv(Sievert). As a unit it is quite large and therefore sub-multiples are used, such as mSv (= 0.001 Sv) [1].

Type of radiation	$\mathbf{w_R}$
Photons (X and γ) of all energies	1
Electrons	1
Protons	2-5
Alpha particles, fission fragments, heavy ions	20
Neutrons	5-20 depending on energy

Table 1.4: Radiation Weighting factor for the evaluation of the H_T Equivalent dose [31].

Part II

MATERIALS AND METHODS

Chapter 2

MATERIALS AND METHODS

2.1 Introduction

Quantitative imaging and dosimetry are crucial for individualized treatment during peptide receptor radionuclide therapy (PRRT).

Combination of molecular imaging and internal radiotherapy targeted at receptors over-expressed in cancer cells is one example of advanced theranostics wherein the pre-therapeutic imaging and radiotherapy are conducted with the same vector molecule, exchanging only the imaging and therapeutic radionuclides. This technique has become a powerful tool for the management of patients affected by Gastroenteropancreatic and neuroendocrine tumorsmoverexpressing somatostatin receptors. One of the main advantages of PET/CT imaging is the possibility of quantifying tracer uptake and kinetics as a reflection of the processes underlying the disease and thus facilitating personalized diagnosis and therapy [26].

GEP-NETS are rare growths that produce peptides and neuroamines, often leading to noticeable clinical syndromes. These tumors originate from enterochromaffin cells and are typically categorized based on their origin from the foregut, midgut, or hindgut. More than half of these tumors belong to the carcinoid category. The development of new diagnostic and treatment methods for these carcinoid tumors could potentially improve the quality of life and extend the survival rate [32].

Somatostatin is a peptide hormone that regulates the endocrine system and affects neurotransmission and cell proliferation via interaction with g-protein coupled SSTRs and inhibition of the release of numerous secondary hormones. High den-

sities of SSTRs are found on many endocrine-related tumors, allowing PET/CT imaging to present higher sensitivity for the detection of well-differentiated GEP-NETs. Imaging the cell membranes who contain somatostatin receptors mainly SSTR2 and SSTR5, not only aids in determine the stage of the disease but also has potential therapeutic benefits [32].

This study provides potential new applications such as quantification of present brain pituitary receptors, and adrenal glands for individualization in theranostics for radionuclide treatment. Thus, we quantitatively investigated the biodistribution of ^{68}Ga-DOTATOC to determine a correlation between the uptake in normal organs such as pituitary and adrenal glands, with the injected dose that is administered for the examination. This information could theoretically be used to modify the therapeutic administered activity of 177-Lu-DOTA]0-D-Phe1-Tyr3-Octreotide (^{177}Lu-DOTATOC).

PET/CT using radiolabeled somatostatin analogs (such as ^{68}Ga-DOTATOC) has been the choice imaging for diagnosis, follow-up, and patient selection for radionuclide therapy because it has higher sensitivity, shorter examination time, higher spatial resolution, and lower radiation dose [33].

2.2 Clinical Utility of Gallium-68

The clinical utility in target- specific ^{68}Ga-based pharmaceutical is particularly notable in the field of nuclear oncology, where it has shown promise for cancer diagnosis, staging, and treatment planning. In ^{68}Ga, the positron has relatively high energy ($E_{max} = 1.9MeV$, $E_{mean} = 0.89MeV$), which allows it to escape from the originating voxel and may lead to lower resolution compared to Fluorine-18 (^{18}F). The spatial resolution is affected by both the energy and the characteristics of the emitted particles. Nevertheless, both computational analysis and experimental measurements have shown comparable image quality for these two radionuclides, given a SIEMENS-scanner and SiPM detector with resolution of 3.2 mm.

On the contrary, $^{68}Ga^{3+}$ can form stable complexes with many ligands containing oxygen and nitrogen as donor atoms. This makes the radioisotope suitable for complexation with chelators and various macro-molecules, allowing for kit development. Targeting SSTR has been notably emphasized as a crucial step in validating

the efficacy of ^{68}Ga-PET agents in clinical applications [34, 35].

The overall reported cases of gastroenteropancreatic-neuroendocrine tumors have risen over the past decades due to changes in detection rate. That implies that improvements in diagnostic techniques, increased awareness, or changes in medical practices have contributed to the observed increase in the incidence of neuroendocrine tumors. In the future, the treatment needs to be individualized for every patient and a better understanding of their biology is mandatory to explore new management options. Somatostatin receptors, mainly SSTR2 and SSTR5 are located on the cell membranes for most of the GEP-NETs. Imaging plays a crucial role not only to determine stage of the disease but has therapeutic implications as well [36].

2.2.1 Radiochemistry- ^{68}Ga-DOTATOC labeling

The ^{68}Ga-DOTATOC was prepared on a fully manual system using a standardized labeling sequence, under the supervision of the head Medical Physicist of the PET/CT Department. The radiopharmaceutical was prepared using a commercially available kit (SomaKit-TOC, Advanced Accelerator Application) containing DOTATOC (edotreotide), a somatostatin analog with a high affinity for SSTR2. Edotreotide labeling was performed following the manufacturer's instructions. Briefly, ^{68}Ga-chloride eluted directly from a ^{68}Ge/^{68}Ga generator **(IRE-Radiopharma Galli Eo)** was added to 40 mg of peptide. The solution was immediately buffered and heated to 95^{o}C for 7 min using a hot plate.

Finally, the product was cooled at room temperature before use, and all steps were performed under sterile conditions. The final product was subjected to thin-layer for high-performance liquid chromatography-HPLC to verify labeling efficiency, and to radio-TLC systems for radioisotope purity. The evaluation of these radiolabeled compounds is conducted by the regulatory authority (INRASTES-Institute of Nuclear & Radiological Sciences and Technology, Energy & Safety) to ensure compliance with safety and efficacy standards.

In all labeling procedures, the radioisotopic purity of ^{68}Ga consistently measured at no less than 92%, while the radiochemical purity remained consistently at no less than 95% [37].

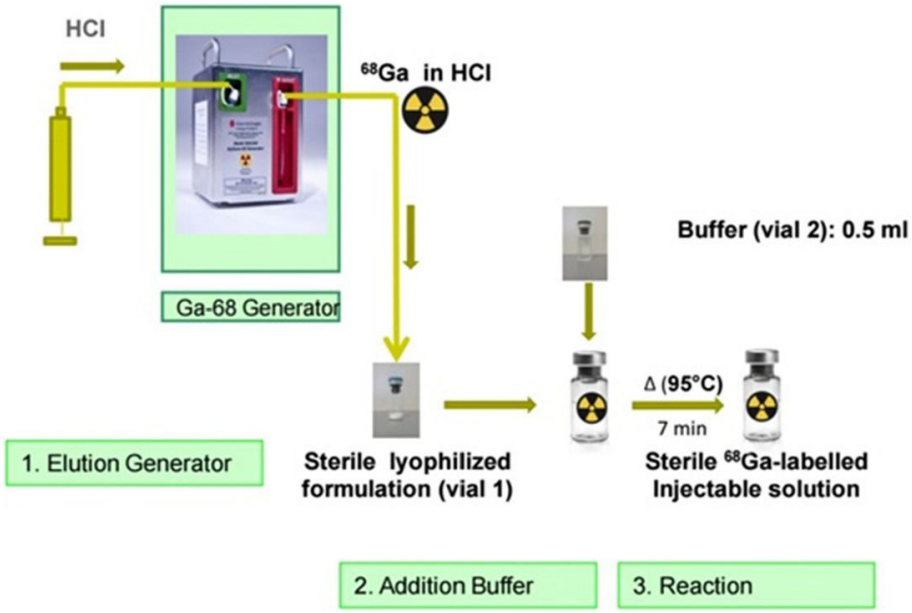

Figure 2.1: Preparation process for Gallium-68 (^{68}Ga).

2.2.2 Dose and mode of administration

The dose of ^{68}Ga-DOTATOC to an adult patient weighting 70 kg is recommended 100 to 200 MBq, administered by direct slow intravenous injection. However, since the labeling and the estimation of the administered dose are done manually, there are some discrepancies or variations. The weight of the patient, amount of dose injected and the estimated time of injection were recorded. The dose was measured using a radionuclide dose calibrator (CAPINTEC CRC-15R). Its reliability ensures consistent and accurate dosage measurements in nuclear medicine. With its high level of accuracy and efficiency it provides precise readings and comprehensive data, allowing clinicians to make informed decisions. After all, ^{68}Ga-DOTATOC was administered intravenously by qualified staff.

Although, it is important to note that in contrast to glucose, gallium exhibits insignificant background uptake, resulting in higher SUV values. This offers notable benefits in diagnosis, as even at low MBq/kg doses, medical imaging is achievable. Also, in Gallium in addition to tumours there is normal-physiological uptake to organs and tissues that are not necessarily pathological regions. It is important to examine these organs that have somatostatin receptors SSTR2 and SSTR5 and understand how they behave [25].

2.3 Siemens Biograph Vision-450 PET/CT System

The Vision-450 integrates a sophisticated imaging system, combining a 128-slice CT scanner with a high-end lutetium oxyorthosilicate PET setup designed for whole-body scans. The system has a large 78 cm bore and an impressive table capacity of 227 kg.

Within the PET component, precision is most important, featuring 8 detector rings and 19 detector electronics assembly units forming a complete ring structure. Each ring comprises 38 blocks, with each block housing a 4×2 array of mini blocks. These mini blocks, in turn, consist of a dense array of $3.2 \times 3.2 \times 20$ mm lutetium oxyorthosilicate crystals coupled with an array of silicon photomultipliers (SiPMs). The SiPM array, measuring 16×16 mm, is equipped with 16 output channels for enhanced sensitivity.

The configuration of these mini blocks, arranged in a 4×2 formation with 2 mini blocks in the axial direction, results in an impressive 32 mm axial field of view (FOV) per block. This detailed regulation, using 8 blocks in the axial direction, reach a finale axial FOV of 25.6 cm, extending to 26.1 cm when considering the packing spaces between the blocks.

The detector's architecture relies on a square array of mini crystals, ensuring complete coverage by SiPM detector components, thereby utilising the maximum potential of SiPM technology. With each crystal measuring 3.2 mm in size, the system achieves great spatial resolution, while the comprehensive coverage maximizes light capture, leading to enhanced timing precision and an elevated signal-to-noise ratio [21].

2.3.1 ^{68}Ga-DOTATOC PET/CT Imaging

PET/CT scans were performed approximately 40-90 minutes after intravenous administration of ^{68}Ga-DOTATOC. Patients voided their urinary bladders immediately before imaging. The measured administered activity was 208.7 Mean +- 64.9 STDEV (Range: 51.8-425.5). After the radiotracer uptake, a CT scan (SIEMENS: 5 mm contiguous axial cuts) was obtained from the vertex to mid-thighs. The CT acquisition was performed in helical mode using 120kV, 512×512 matrix, and field of view of 867 mm in 22.5 seconds. No oral or intravenous contrast material was

Figure 2.2: SIEMENS Biograph Vision-450 PET/CT System

used. The CT scan was used for attenuation correction purposes and for anatomical localization of the radiopharmaceutical.

As for the Effetctive mAs, SIEMENS has an automatic exposure control system AEC in CT. The system is called CARE Dose4D and it employs automatic adjustment of tube current in both angular and longitudinal dimensions, also flexibly adapting to diverse anatomical regions and patient sizes. In CARE Dose4D, a technique parameter is calculated by dividing the actual tube current–time product (mAs) by the spiral pitch value. This parameter is automatically determined by the system based on factors such as the selected Quality Reference mAs (QRM), the topogram, and the chosen scan protocol. Before the scan, the estimated average effective mAs is displayed, which may differ from the prescribed QRM. After the scan, this value is updated to reflect the actual average effective mAs used, which may vary slightly due to CARE Dose4D adjusting pre-scan estimated values with more accurate values from the scan acquisition [38].

Immediately after the CT, an emission PET scan was acquired over the same anatomical regions. The PET emission scan was corrected using SAFIRE (Sinogram Affirmed Iterative Reconstruction) which is a unique CT iterative reconstruction algorithm that uniquely allows for up to 60% lower radiation dose in CT examinations without compromising image quality [39].

2.3.2 Image Evaluation

This evaluation refers to the process of analyzing and interpreting the images obtained from the scan. It is typically performed by experienced radiologists and nuclear medicine physicians, responsible for evaluating the images to identify any abnormalities, lesions, or areas of interest. During image evaluation, various factors may be considered, including the distribution and intensity of radiotracer uptake, the anatomical location of abnormalities, and any correlation with other diagnostic findings.

The imaging examinations reveal increased radiopeptide uptake in three non-pathological regions, specifically: 1) the pituitary gland within the brain, 2) the right adrenal gland, and 3) the left adrenal gland. Only regions showing a physiological corresponding structure on the CT scan portion of the full-dose PET/CT or on subsequent examinations were taken into account. If either of the two adrenal glands exhibited any form of abnormality, the patient would not be included in the study. The same criterion would be applied if there were any imaging issues with the pituitary gland.

Thus, this method of analysis was applied to 160 patients who underwent a full-dose PET/CT scan. SUV measurements were conducted on areas within fused image datasets. Spherical volumes of interest were delineated closely around regions of interest, from which the $SUVmax$ and $SUVmean$ were collected [40].

2.4 The pituitary in Nuclear Medicine Imaging

GEP-NETs constitute a heterogeneous group of neoplasms that have been postulated to originate from a common precursor cell population. The system includes endocrine glands, such as the pituitary, the parathyroid, and the (neuroendocrine NE) adrenals, as well as endocrine islets within glandular tissue (thyroid or pancreas) and cells dispersed between exocrine cells, such as endocrine cells of the digestive and respiratory tracts, and the diffuse endocrine system. Because these cells share a number of antigens with nerve elements, the term ‘neuroendocrine’ is also used to denote such cell types. GEP-NETs possess neuroamines uptake mechanisms and/or specific receptors at the cell membrane, such as somatostatin receptors, which can be of great value in identifying and localizing these tumors as well as being useful

in their therapy.

Pituitary is part of the endocrine system, it releases several important hormones and controls the function of many other endocrine system glands. The anatomy of the pituitary gland is divided into two independent parts, the anterior pituitary (frontal part) and the posterior pituitary (rear part). Despite its small size, the pituitary gland influences nearly every part of the body. The hormones it produces help regulate important functions such as growth, blood pressure, menstruation in females, and reproduction.

- The anterior lobe of your pituitary gland makes and releases the following hormones: Adrenocorticotropic hormone (ACTH or corticotrophin), Follicle-stimulating hormone (FSH), Growth hormone (GH), Luteinizing hormone (LH), Prolactin, Thyroid-stimulating hormone (TSH).

- The posterior lobe of your pituitary gland stores and releases the following hormones, but your hypothalamus makes them: Antidiuretic hormone (ADH, or vasopressin), Oxytocin.

In the central nervous system, all subtypes of somatostatin receptors are expressed, while there are specific regions with distinct expression patterns for each subtype. In the pituitary gland, all somatostatin receptors are expressed in varying proportions:

$$\text{SSTR2} > \text{SSTR1} = \text{SSTR3} > \text{SSTR5} > \text{SSTR4}$$

The ^{68}Ga-DOTATOC (a somatostatin analog, labeled with gallium-68) has a high affinity for SSTR2, and its uptake can be expressed in SUVmean. Functional imaging using radiolabeled somatostatin analogs has emerged as a diagnostic and follow-up modality of well-differentiated NETs that also express somatostatin receptors and helps to select the best therapy for these patients.

We have collected clinical data through medical records of Biomedical Research Foundation Academy of Athens (BRFAA), for the acquisitions of ^{68}Ga-DOTATOC PET/CT images to correlate the Injected Activity with the radiopharmaceutical uptake in the region of pituitary and in the region of the adrenal glands [41, 42].

2.4.1 CT Characteristics of the Normal Pituitary gland

The pituitary is an endocrine gland with ability to uptake diverse radiopharmaceuticals and, therefore, can be investigated by nuclear medicine diagnostic procedures. The pituitary gland (also known as hypophysis) is a small pea-sized gland located at the base of the brain, below the hypothalamus. The adult gland has an anteroposterior diameter $\approx$ 8 mm and a transverse diameter $\approx$ 12 mm.

That being said, with reference to research findings derived from CT scans, it has been established that the diameter of the pituitary gland is larger in women compared to men. Also, the gland height it is affected by the age and the gender. The older you get the pituitary gland tend to decrease in size progressively (referring to ages over 18 years old). However, the relationship between the gland size, age, and gender is complex [42, 43].

Sex differences in gland height

In females, the pituitary gland is influenced by multiple factors. The gland height increases during periods of fertility in women and puberty due to hormonal activities. But, the activity of the pituitary gland decreases at menopause due to the decline in the production of reproductive hormones, particularly estrogen and progesterone, which are regulated by the hypothalamus-pituitary-gonadal axis.

For males, due to the absence of an ovulatory cycle and the delayed appearance of andropause, along with minimal changes in hormones and their organism, the size of the pituitary gland remains relatively stable [44].

2.4.2 Pituitary uptake on ^{68}Ga-DOTATOC PET/CT

^{68}Ga-DOTATOC is used in PET examinations targeting somatostatin receptors in patients affected by neuroendocrine tumors. Somatostatin is a peptide hormone that regulates the endocrine system and affects neurotransmission and cell proliferation via interaction with g-protein-coupled SSTRs and inhibition of the release of numerous secondary hormones. SSTR receptors have been described in the brain, but ^{68}Ga-DOTATOC cannot cross the blood–brain barrier.

The pituitary gland uptake in normal tissues has shown that is the fourth organ with the highest uptake, only after the spleen, kidneys and adrenal glands. The

use of ^{68}Ga labeled PET tracers has increased, due to their convenient preparation using a ^{68}Ge/^{68}Ga generator. High potential for imaging of somatostatin receptor - positive gastroenteropancreatic neuroendocrine tumors with ^{68}Ga-labeled octreotide has been well demonstrated. SSTR has several major subtypes and due to the unequal distribution of the subtypes in SSTR-positive malignancies the structures of the somatostatin analogs are varied to obtain high binding affinity.

^{68}Ga-DOTA (1, 4, 7, 10-tetraazacyclododecane-1, 4,7, 10-tetraacetic acid) labeled somatostatin analogs are positron-emitting tracers with high sensitivity and specificity for detection of SSTR and can provide a more thorough and conclusive evaluation of NET.^{68}Ga-labeled DOTATOC (DOTA-D-Phe1-Tyr3-octreotide), DOTATATE (DOTA-Tyr3-octreotate) and DOTANOC (DOTA-1-Nal3-octreotide) are commonly used radiotracers for PET imaging of NET.

The SUVmax in PET/CT with ^{68}Ga-DOTATOC corresponds to receptor density on the shell surface and is measurement of biological significance of GEP-NET lesions rather than tumor metabolism as in ^{18}F-FDG. In this study, for the BRFAA we used ^{68}Ga-DOTA-Phe1-Tyr3-octreotide (TOC), which has a high affinity for SSTR2 and SSTR5 [45].

2.5 The Adrenal glands in Nuclear Medical Imaging

Regarding the anatomy of the organ, the right adrenal gland is forming a triangular shape, is posteriorly related to the diaphragm and anteriorly to the inferior vena cava and liver. Positioned within the left diaphragmatic crux, the semi-lunar left adrenal gland is separated from the stomach by the omental bursa. It also related with the spleen and pancreas.

The adrenal cortex consists of three distinct layers, each responsible for secreting unique steroid hormones. The exterior layer, *zona glomerulosa* produces mineralocorticoids, most importantly, aldosterone, regulating salt and water metabolism. The middle layer or *zona fasciculata* produces the glucocorticoids, particularly cortisol. And the innermost layer, *zona reticularis*, the adrenal androgens DHEA, DHEAS-S and androstenedione [46].

The adrenal glands exhibit a higher density of SSTRs in the tissue compared to the pituitary gland. Consequently, larger quantities of pharmaceuticals are ab-

sorbed, as somatostatin receptors play a crucial role in the targeted imaging and treatment of certain neuroendocrine tumors.

The adrenal gland may show a wide variety of pathologic conditions, including benign adenomas, adrenal malignancies, and metastatic diseases. So, it is crucial to conduct an investigation into the normal appearance of the adrenal glands. A number of imaging techniques can be used to characterize these, although it is not always possible to attain a definitive diagnosis radiologically. Hence, an appreciation of the complexities of adrenal imaging strategies and characterization is required.

When evaluating adrenal glands at PET/CT you have to consider other radiologic features, including the size of adrenal nodules, the presence of fat or calcification, the attenuation of nodules and atypical imaging features. In cases of known endocrine activity in combination with imaging features, we can guide clinical management [47].

2.5.1 CT characteristics of the Adrenals

CT is the primary diagnostic imaging modality utilized for the characterization and detection of adrenal masses due to high lipid content and therefore low attenuation values on un-enhanced CT scans. The normal adrenal gland is larger than the spatial resolution of PET, however it is usually barely visible only on PET scan. Combined PET/CT image can reach beyond the morphological level into the molecular characteristics of adrenal lesions. The fused image visualizes the metabolic activity with the morphological information corresponding to normal uptake in the location of the glands identified on the co-registered CT scan [46].

2.5.2 Adrenal gland uptake on ^{68}Ga-DOTATOC PET/CT

Significant uptake of radiolabeled somatostatin analogue ^{68}Ga-DOTATOC was seen in all patients. SSTR receptors have been described in the spleen, liver, pituitary gland, adrenal glands, and in the urinary tract (kidneys and urinary bladder). Adrenals are the third organ with the highest concentration of ^{68}Ga-DOTATOC after the spleen and kidneys.

In this study, were included only the adrenals which were proven to have no pathology by either conventional radiological imaging and/or on clinical follow up

based on the assessment of the Nuclear medicine doctor. Normal range of $SUVmax$ and $SUVmean$ were calculated for the following adrenal glands. Uptake in the adrenal glands follows their morphologic appearance presenting as a little triangular pattern. The uptake was evaluated using regions of interests (ROI) in all three dimensions. Initially they were drawn based on the CT scan, and then were implemented for corrections and adjustments with the fused PET scan.

Radiopeptide normal uptake in the adrenal glands typically is demonstrating as a symmetrical uptake (defined as a difference in SUVmax of no more than 20%). The SUVmax was recorded as 13.9 in the right adrenal gland and 14.1 in the left adrenal gland. Statistical analysis did not reveal a significant difference in uptake between the left and right adrenal glands [46].

2.6 Imaging on SIEMENS Biograph Vision-450 PET/CT

Half-body PET/CT examinations from vertex to the upper thighs were performed on a Biograph Vision PET/CT scanner (Siemens) using 3-dimensional mode.

All patients were requested to drink 1.5 L of water for hydration and empty their bladder before the PET/CT examination. Patients were positioned supine with the arms raised according to standard CT practice. A low-dose CT scan was acquired continuously in spiral mode using 120 kV, automatically determined mAs (CARE Dose4D), 5 mm slice thickness, and a pitch of 0.8. In the same position, the PET study was acquired covering an area identical to that cover by CT at 1.5 minutes per bed position (7-8 bed positions depending on the size of the patient).

Emission data were reconstructed on a 168 x168 matrix using ordered-subsets expectation maximization algorithm (3 iterations, 21 subsets) and corrected for attenuation using the low-dose CT. The PET/CT images (half-body-attenuated and no attenuated PET, CT, and fused images) were transferred to a multimodality work station [MMWS; Syngo (TrueD); Siemens Medical Solutions] for analysis [21].

2.6.1 Image Analysis

Image analysis was performed on the LIFEx v7.4.0. **LIFEx** (Local Image Features Extraction) is a software for radiomic feature calculation in multimodality imaging. DICOM images were taken after the Siemens Biograph Vision-450 PET/CT scan at BRFAA, and were imported in the software for further analysis. Organs of interest for our study, known to have expression of somatostatin receptors were identified on the component of the PET/CT scan.

We examined the pituitary and the adrenal glands, incorporating the radiomic analysis (feature extraction) for each patient as well. The uptake was evaluated using Volumes of interest (VOIs) applied in the attenuation- corrected PET slices, and drawn around the whole organ for small structures such as the pituitary and the adrenal glands. $SUVmax$ was defined as the single pixel with the highest value within a Volume of Interest. $SUVmean$ was taken as the average SUV concentration in VOI. $SUVmax$ and $SUVmean$ were evaluated on axial, coronal and sagittal images in two areas of normal physiological structures for each patient, avoiding inclusion of any activity from adjacent organs [48].

2.6.2 LIFEx v7.4.0

LIFEx is a software capable of interpreting medical images, whether stored locally or accessed via a network, through a DICOM browser (it is specifically designed for DICOM images). It runs well on Windows10, Windows11, MacOs (Mojave, Catalina, Big Sur, Monterey, Ventura (available on M1 or M2 ARM processors)) and Linux/Ubuntu, Debian, Fedora distributions (.rpm, .tar, .deb). In terms of functionality, LIFEx provides a lot of unique features, including a dynamic 3D-reconstruction based slice viewer. Many research laboratories, radiology departments, and medical facilities utilize it for analyzing textural features and identifying tumors.

The medical images analyzed by LIFEx typically originate from Computed Tomography or Positron Emission Tomography scans, with Magnetic Resonance Imaging (MRI) scans being less common. A huge variety of textural indices is given, which are associated with the number of gray levels (existing in the image) and their distribution (spatial or not)/ frequency/ etc. These indices are extracted from specific customizable set of volumes, named regions of interest (ROIs), which can be

imported from an already existing file. Results are exported to Excel or cvs format files, ready to be processed.

Overall, LIFEx serves as a valuable freeware tool for radiomic feature calculation, empowering the medical community to accelerate advancements in the characterization and understanding of tumor heterogeneity, ultimately leading to improved diagnostic accuracy and patient outcomes [49].

Regions Of Interest

Criteria for radiomic feature selection include carefully defined ROIs for post-processing and feature extraction. Every ROI is a customizable area, which is used for textural analysis. In our study, each and every ROI is a 3D area (VOI) incorporating a minimum of 64 voxels, identified manually under the supervision of a radiologist. ROIs should be singular entities, contained of connected voxels. Nevertheless, it's possible for an ROI to consist of multiple clusters of voxels. In such cases, textural features or indices are only derived from the largest cluster. The method by which an ROI is defined is critical, as certain attributes (such as potential edges) can significantly influence both textural and conventional index values [50].

Setting a Region Of Interest

It is essential to define a region of interest that represents a specific volume within the 3D animation. Which is obtained through one of the compatible medical imaging protocols on PET/CT scans. The ROIs may be 2D or 3D, but in 2D ROIs many textural indices cannot be used for calculations. Because of the previously mentioned point, we utilized 3D ROIs that had numerous of tools accessible.

Thus, the Volume of Interest was drawn with a Circle 3Dd tool. A size-adjustable 3D circle can be placed upon the area of interest(size of circle is quantized – specific pre-built in sizes are available, because its circle is made of voxels). The size of circle may be manipulated by pressing shift key and rolling mouse wheel and placed by pressing shift key and left (mouse) click.

Other tools that can be used for 3D-ROI modification are [50, 51]:

- Copy tool (copies the selected ROI)
- FlipAP tool (copies and flips the selected ROI to anterior or posterior side)

- FlipRL tool (copies and flips the selected ROI to left or right side)
- FlipIS tool (copies and flips the ROI anti-diametrically),
- Fill 3D tool (fills the empty volume of the selected ROI),
- Dispose tool (deletes selected ROI),
- Union tool (connects different ROIs to a single one),
- Split tool (splits different clusters of voxels of a single ROI to a lot of ROIs, each cluster is a new ROI),and
- Interpolation tool (measure the empty volume between two clusters of voxels, which belong to the same ROI).

2.6.3 Standardized Uptake Values

The localized metabolic activity can be quantified as a Standardized Uptake Value (SUV). It's computed by dividing the concentration of radioactivity in tissues by the injected dose of the radiopharmaceutical, with normalization typically to body weight or body mass index. This normalization allows standardized comparisons across patients, regardless of their size or the exact amount of the radiopharmaceutical administered.

It is commonly used by nuclear medicine professionals to differentiate between normal and abnormal levels of uptake. Abnormal uptake patterns can indicate the presence of disease, such as cancer or inflammation. The uptake was evaluated using regions of interest (ROI) drawn around the whole organ in axial, coronal and sagittal projections for the pituitary gland and the adrenal glands.

An approximately circular VOI of $2.00cm^3$ was drawn for the pituitary gland. Regarding the adrenal glands, a triangular volume of interest (VOI) measuring approximately $4.76cm^3$ for the left adrenal, and similarly, for the right adrenal a VOI of $4.38cm^3$ was delineated as well. We collected all SUV indices (SUV_{max} , SUV_{mean}, SUV_{median} , SUV_{min}) but placed emphasis on the SUV_{mean} as we consider it to be more indicative of the tissue, given its health and normality.
The SUV_{max} and the SUV_{mean} were calculated in all ROIs using the following formulas:

$$\mathrm{SUV}_{\mathrm{max}} = \frac{\text{maximum activity concentration at time from pixel values}}{\text{injected dose/patient body weight}}, \tag{2.1}$$

$$\mathrm{SUV}_{\mathrm{mean}} = \frac{\text{mean activity concentration at time from pixel values}}{\text{injected dose/patient body weight}}. \tag{2.2}$$

Overall, because we examine healthy tissues in addition to SUV indices, we need some features that can help uncover subtle differences within tissues and potentially provide complementary information to SUV measurements. Combining SUV indices with image analysis, a more comprehensive understanding of tissue characteristics and potential disease presence can be achieved [52].

2.7 Radiomics - feature extraction

Medical image analysis has transformed images originally intended exclusively for visual interpretation into extractable data through a practice known as "radiomics." Artificial intelligence has further advanced the application of PET/CT radiomics. It is defined as the "high-throughput extraction of quantitative features that result in the conversion of images into mineable data", and feature prominently in what is today called "quantitative imaging" [53]. The feature extraction has a large number of quantitative features from the images using high-performance automated methods. The quantitative features of the images provide information regarding the phenotype and the micro-environment of the tumor based on intensity, shape, size, volume, and texture of the region of interest [54].

The information provided by radiomics involves spatial and textural patterns in the grayscale and describes the relationship between pixels or voxels in an image. The use of radiomics can expand the boundaries of visual assessment, it is a tool that characterizes the heterogeneity of tumors through PET/CT images. LIFEx v7.4.0 calculates every image feature under the regulations of IBSI (Image Biomarker Standardisation Initiative). IBSI is an autonomous global alliance focused on standardizing the process of extracting image biomarkers from obtained images for high-throughput quantitative analysis of images (radiomics). Overall,

there were over 200 textural features extracted from the DICOM image provided by the software. Below, we will describe the indices that were statistically significant, in consideration of the analysis conducted [52].

2.7.1 Volume

The mesh based Volume it is computed from the net of the Region of Interest (ROI) in the following manner. A tetrahedron is created by each face k and the origin. When positioning the origin vertex of each tetrahedron at coordinates (0,0,0), the volume of the tetrahedron, taking into account its orientation, can be determined as:

$$V_k = \frac{a \cdot (b \times c)}{6}. \tag{2.3}$$

Here a, b, and c represent the vertex points of face k. The signed volume depends on the orientation of the normal, resulting in either a positive or negative value. Therefore, it's crucial to ensure consistency in the orientation of face normals. For instance, all normals should either point outward or inward. The volume V is obtained by summing the volumes of all faces and then taking the absolute value to ensure a positive result.

$$F_{\text{morph.vol}} = V = \left| \sum_{k=1}^{N_{\text{fc}}} V_k \right|. \tag{2.4}$$

In clinical settings, volumes are often calculated through voxel counting. For volumes containing numerous voxels (in the thousands), discrepancies between voxel counting and mesh-based methods are typically insignificant. Yet, for volumes comprising fewer voxels (tens to hundreds), voxel counting tends to overstate volume in contrast to mesh-based techniques. Consequently, the voxel count serves simply as a reference tool and is not employed in computing other morphological features. ***Voxel counting*** is expressed as:

$$F_{\text{morph.vol}} = V = \sum_{k=1}^{N_\upsilon} V_k. \tag{2.5}$$

Here, N_υ represents the voxel count within the morphological mask of the ROI, while V_k denotes the volume of each voxel.

$\mathbf{X_{gl}}$ index

$\boldsymbol{X_{gl}}$ represents the set of voxel intensities extracted from the intensity mask of the ROI. In this context, the term "mask" refers to a binary image that delineates a specific region or structure of interest within a larger image. The mask is essentially a map that highlights which pixels or voxels belong to the region of interest and which do not. It acts as a filter, allowing selective analysis or manipulation of the designated area while excluding irrelevant background information [52].

2.7.2 Intensity-based statistical features

The statistical characteristics based on intensity, describe the distribution of intensities within the region of interest. These features do not require calibration and can reflect a continuous spread of intensity. However, these statistical properties lose their significance if the intensity scale is not standardised. They are used in image processing, computer vision, and pattern recognition tasks to characterize the texture, structure, and other visual properties of an image.

These features are often used as input for machine learning algorithms in tasks such as image classification, object recognition, and image acquisition. By quantifying different aspects of the intensity distribution, they provide valuable information about the visual content of the image, which can help in distinguishing between different classes or categories of images [52].

Mean intensity

The mean intensity of X_{gl} is calculated as:

$$F_{\text{stat.mean}} = \frac{1}{N_v} \sum_{k=1}^{N_v} X_{\text{gl},k} \tag{2.6}$$

Maximum intensity

The maximum intensity corresponds to the highest intensity value within X_{gl}, and is given by

$$F_{\text{stat.max}} = \max(X_{\text{gl}}). \tag{2.7}$$

Standard deviation (SD)

The intensity variance of X_{gl} is described as:

$$stand.deviation = \sigma = \frac{1}{N-1}\sum_{i=1}^{N}(X_{gl,i} - \bar{X})^{1/2}. \tag{2.8}$$

Coefficient of Variation

The coefficient of variation quantifies the spread of X_{gl}. It is expressed as:

$$F_{\text{stat.cov}} = \frac{\sigma}{\mu}. \tag{2.9}$$

and it shows the extend of variability in relation to the mean of the population.

Intensity-based Energy

The energy is defined as:

$$F_{\text{stat.energy}} = \sum_{k=1}^{N_v} X_{\text{gl},k}^2. \tag{2.10}$$

2.7.3 Grey level co-occurrence Matrix-based features

The grey level co-occurrence matrix (GLCM) is a representation showing the paired scaled intensities (grey levels) are distributed between adjacent pixels or voxels within a 3D volume. Typically, the GLCM considers a 26-connected neighborhood with 13 unique direction vectors for the Chebyshev distance δ=1. The δ-index value is the average of the index for the number of different directions. From this matrix, seven texture indices are computed and they are calculated for each direction vector.

The GLCM contains information regarding the arrangement of voxels with similar grey level values. Essentially, it illustrates the spatial distribution of co-occurring pixel values at a specific offset. Typically, the offset value is set to 1 (although it can range up to 10), indicating that only the relationship between neighboring voxels is considered – a preference when examining tumors. If the distance is too extensive for small Regions of Interest (ROIs), certain entries in the GLCM may become meaningless, resulting in NaN (Not a Number) or Num (Number) outputs [52].

Entropy

$\text{GLCM}_{Entropy}$ quantifies the unpredictability of grey level voxel pairs, serving as a guide to the content of the information.A high entropy matrix indicates an image where no specific grey levels are selected for the distance vector δ [52].

Difference Entropy

Difference entropy for diagonal probabilities [Haralick1973] is characterized as:

$$Fcm.diff.entr = -\sum_{k=0}^{Ng-1} p_{i-j,k} \log_2 p_{i-j,k}. \tag{2.11}$$

Sum Entropy

The cross-diagonal probabilities' sum entropy, as defined in [Haralick1973], is characterized as:

$$Fcm.sum.entr = -\sum_{k=2}^{Ng} p_{i+j,k} \log_2 p_{i+j,k}. \tag{2.12}$$

2.8 Statistical Analysis

Statistical analysis was performed using Excel and SPSS Statistics 26. In order to examine the association between SUV indices with each body weight and injected activity, Pearson's rank correlation coefficient was used to assess the correlations between parameters. A p-value of less than 0.05 was assumed to be statistically significant. Graphs were drawn using Excel and SPSS v.26.

Part III

RESULTS

Chapter 3

RESULTS

3.1 Patient characteristics

One hundred sixty (160) patients (79 men, 81 women; mean age, 59 ±14 y; age range: 22-90 y) referred for imaging using ^{68}Ga-DOTATOC PET/CT at BRFAA, were included in the study. Clinical history and treatments were documented. Patients underwent examination either at the time of initial diagnosis or throughout the course of their illness, with some being reexamined during follow-up, establishing the diagnosis of GEP-NETs. From these patients, sites of physiological uptake were identified and confirmed to be disease-free for our study.

The patients were classified into two groups based on the area of interest under study. The first group consists of patients who are disease-free at the time of examination since we focus on the pituitary gland. The second group consists of patients who, in addition to having healthy pituitary gland, they also have healthy adrenal glands. This implies that the number of patients in the second group is smaller since we have introduced an extra condition. There were three reasons for the decreased number of patients in the second group. First, one of the adrenal glands couldn't be identified due to prior surgical removal. Second, a tumor was present at the adrenal glands. Third, it was challenging to visually distinguish the adrenal glands from adjacent organs during either the PET or CT portions of the examination.

The third reason for excluding patients occurs when a person is very thin. In these cases, where there is a lack of fat in the body, the organs may appear closer together, making it difficult to identify and separate them. The fat acts as a kind

	Characteristics						
	No.of patients	Age(y)		Sex		ROI	
		Mean±SD	Range	Male	Female	Pituitary	Adrenal glands
Data	160	59±14	22-90	79	81	160	135 pairs

Table 3.1: The table presents the characteristics of the patients.

of contrast mediator that helps to separate the organs. This can lead to difficulty in interpreting the image and evaluating the results of the examination.

Patient selection was facilitated in collaboration with the Nuclear Physician and the Radiologists from BRFAA. The examination starts sixty minutes after the intravenous injection of ^{68}Ga-DOTATOC at a dose of 208.7± 64.9 [MBq], patients underwent PET/CT imaging utilizing the SIEMENS Biograph VISION-450 PET/CT system with SiPM crystals and TOF=214ps.

3.2 Pattern of physiological uptake

In the typical distribution pattern of ^{68}Ga-DOTATOC there is usually noticeable physiological uptake in the spleen, liver, both kidneys, both adrenal glands, and the pituitary gland. When it comes to organs such as the adrenal glands and the pituitary, ROIs were delineated manually, covering the entire organ volume based on the most accurate visual estimation of the organ boundary on the PET/CT images, as previously detailed. SUV parameters were evaluated for the organs considered non-pathological.

Specifically, the SUVmean and SUVmax were used to compute the various mean and maximum specific activity uptake. In the case of the adrenal glands, values were derived individually for each gland, as well as the combined mean value for both the right and left glands. The volume of interest affects the concentration of activity in the adrenal glands, due to variations in their sizes, which are dependent upon the patient's anatomy [55]. The physiological distribution of SUV indices for the organs of interest are summarised in the table below.

Descriptive Statistics							
Organ	**Mean**	**Std. Dev**	**Min**	**Max**	**Percentiles**		
					25th	*50th (Median)*	*75th*
Pituitary gland	3.15	0.88	1.80	6.62	2.54	2.99	3.65
Left Adrenal gland	9.82	2.09	5.07	14.29	8.50	9.83	11.36
Right Adrenal gland	9.16	1.96	4.84	13.93	7.78	9.12	10.66

Table 3.2: The table presents the AVERAGE of the SUV indices

3.3 ROIs drawn using the LIFEx v7.4.0 software

The CT transmission images were employed to correct for attenuation in the PET emission data. Following corrections for scatter and attenuation, the PET emission data underwent reconstruction using the SAFIRE algorithm. SAFIRE is a unique CT iterative reconstruction algorithm that uniquely allows for up to 60% lower radiation dose in your CT examinations without compromising image quality [39].

The PET/CT image analysis was perfomed on LIFEx software, LIFEx can directly load DICOM images. Focal regions showing normal uptake of ^{68}Ga-DOTATOC in the pituitary and adrenal glands, which presented stable morphology or structure on the corresponding PET/CT images, were counted as positive. A ROI was delineated for each specific gland using a manual segmentation technique, which includes the outline of a 3D-region around the organ. This method groups all the adjacent voxels within a drawn circle in the image. In addition, through textural analysis of each VOI, numerous parameters have been identified. Our study will mainly focus on analyzing the parameters that exhibit significant correlations with the $SUVmean$ index. These parameters include the maximum Standardized Uptake Value (SUVmax), Sex (SEX), Coefficient of Variation (CoV), as well as Energy,

Sum-Entropy, and Difference-Entropy.

Apart from analyzing tumor lesions, we examined normal organs with high physiological uptake. This allowed us to obtain measurements for the parameters of interest within the standardized VOIs. The pituitary gland will be analysed using VOIs of similar size, while the entire adrenal glands will be evaluated using variable VOIs tailored to each patient's anatomy.

Pituitary gland

PET images allow us to observe the metabolic activity of tissues. As for the pituitary gland located inside the brain, stands out for its highly increased uptake of the ^{68}Ga-DOTATOC. This distinctive characteristic makes it a prominent region of interest in PET imaging not only for evaluating its functionality, but also for confirming that the labelling of the radiopharmaceutical has been done correctly.

The regions of interest for the pituitary gland are visible below on the PET, CT, and fused PET/CT images using the LIFEx v7.4.0 software.

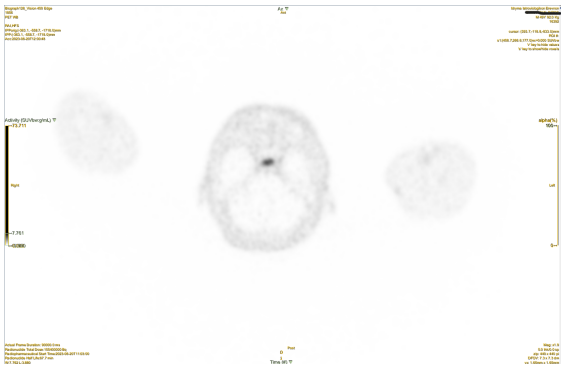

Figure 3.1: Axial projection of a normal pituitary gland on the PET image.

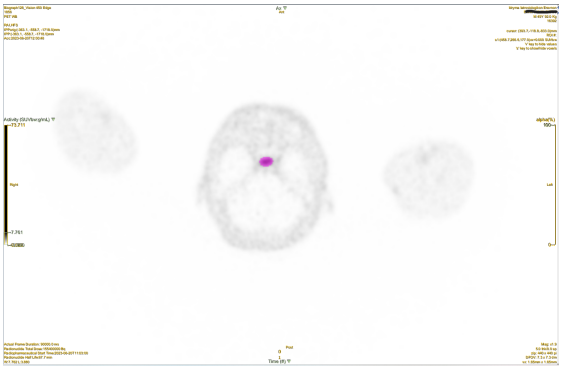

Figure 3.2: Same axial projection, with the ROI drawn on the PET image.

ROIs are outlined in all three anatomical views: axial, coronal, and sagittal projections, effectively defining a VOI for the organ under study. In particular, the VOI for the pituitary is represented in the ^{68}Ga-DOTATOC PET scan. PET scan reveals areas of metabolic activity, while the CT scan provides anatomical context. The VOI designed for all patients has an approximate consistent volume of 2 cm^3, aiming to avoid any potential errors in the statistical analysis of the gland.

In Figure 3.4, the ROI is drawn in the axial projection of the pituitary gland on a CT image. Nevertheless, pituitary is a glandular tissue, which can sometimes be

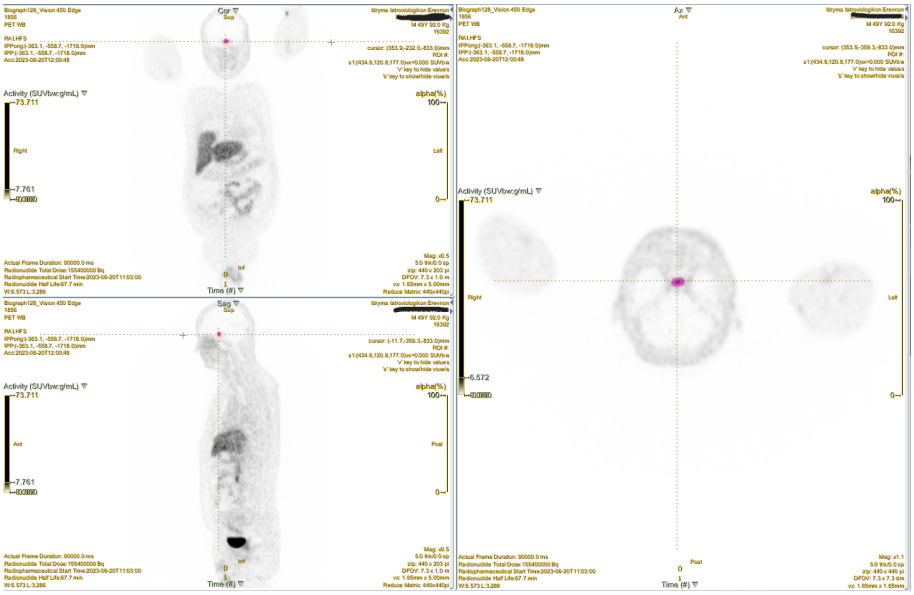

Figure 3.3: ROIs delineated in all projections on the PET image: axial, coronal, and sagittal.

challenging to visualize clearly on conventional CT imaging due to their soft tissue composition, resulting in low X-ray attenuation. As a result, pituitary appears as dark area on CT images, lacking the contrast for clear visualization. The most effective methods for imaging the pituitary gland involve techniques such as contrast-medium (CM) CT or MRI. However, by using PET scan, the regions of increased metabolic uptake in the brain corresponds to pituitary tissue, so this method is the only one that helps identify the gland's location in the images.

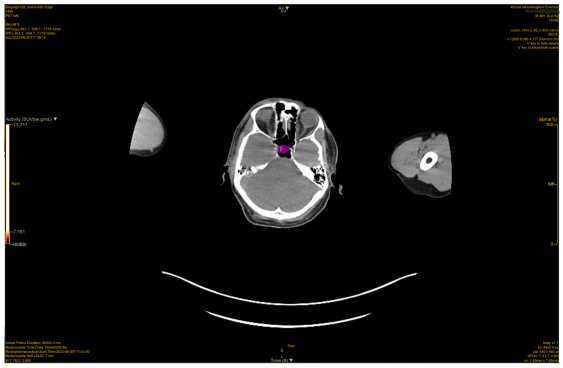

Figure 3.4: A ROI drawn in the axial projection of the pituitary gland on the CT image.

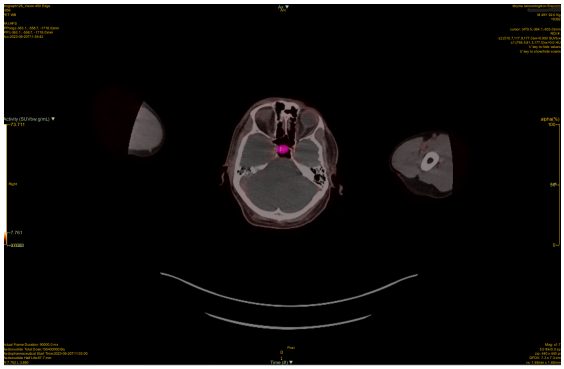

Figure 3.5: A ROI delineated on the axial projection of the pituitary gland on the fused PET/CT image.

Overall, observing the metabolic uptake in the pituitary tissue on PET/CT scans can aid valuable insights into various physiological and pathological processes oc-

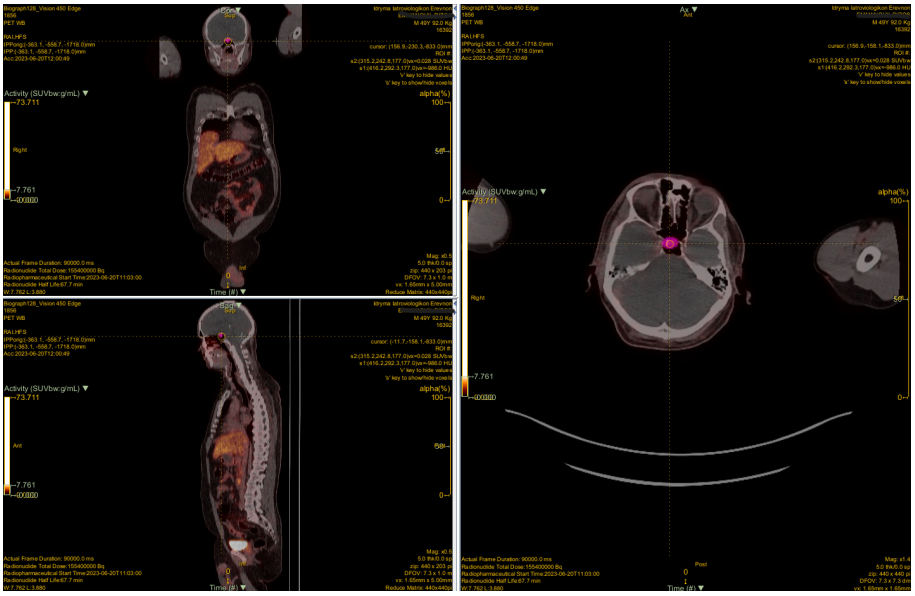

Figure 3.6: ROIs delineated in the axial, coronal, and sagittal projections of the pituitary gland on the fused PET/CT image.

curring in the gland. However, sometimes relying on a single uptake index may not always provide a comprehensive understanding of tissue behavior. Moreover, certain pathologies may remain undetected even by the trained eye of the Radiologist. Therefore, we need specific textural features of the image to help us in observing the gland's behavior. In LIFEx v7.4.0, textural features can be extracted from the PET image and stored in a CSV file for each patient, along with the corresponding regions of interest (ROIs) delineated in the image [56, 57].

Adrenal glands

The ROIs of the adrenal glands are also illustrated in the followings CT, PET, and PET/CT images. Although the normal adrenal glands overcomes the spatial resolution limit of PET imaging, initial delineation of the ROIs within the glands is conducted on CT images to ensure precise identification.

After the initial delineation on the CT images, additional refinement can be performed on the corresponding PET images to optimize the accuracy of the ROIs. This multi-step approach enhances the reliability of the measurements and facilitates comprehensive analysis of metabolic activity within the adrenal glands.
The procedure is followed in order to properly evaluate the standard uptake values.

In the images, homogeneous uptake in both the left and right adrenal glands is

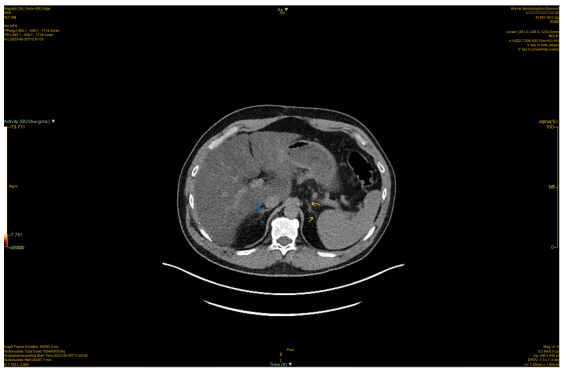

Figure 3.7: Axial projection of the adrenal glands on the CT image.

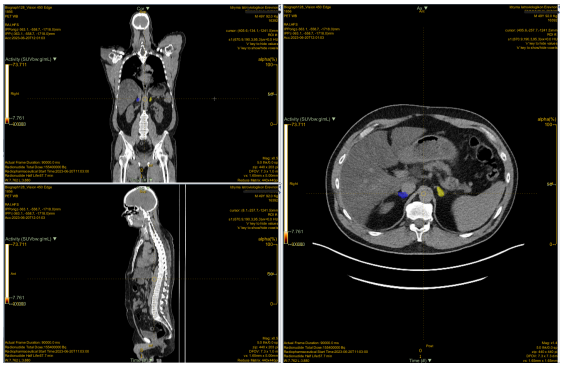

Figure 3.8: ROI is drawn in all projections of the adrenal glands on the CT image.

essential to ensure their normal function. Different intensities of SUV values may indicate potential differences in metabolic activity or tracer uptake, providing valuable information about the physiological or pathological status of these glands. This information is critical for the diagnosis and management of endocrine disorders, assisting in treatment planing and patient management.

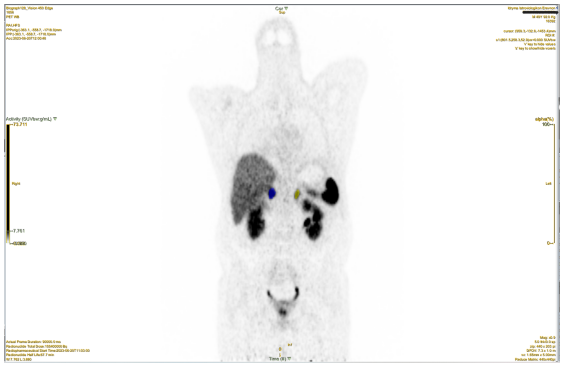

Figure 3.9: ROI is drawn in the coronal projection of the adrenal glands on the PET image.

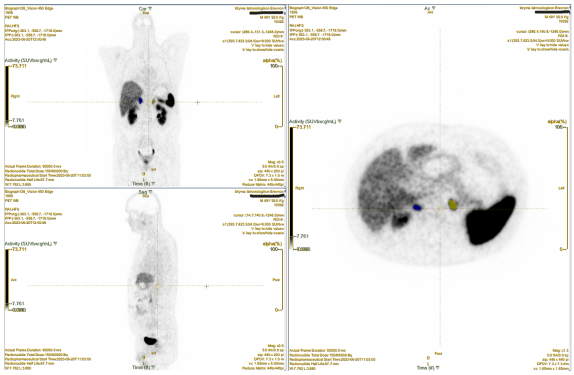

Figure 3.10: Every ROI in axial, coronal, and sagittal projection of the adrenal glands on the PET image.

Afterwards, corrections are applied to the fused PET/CT images to further refine and enhance the accuracy of the SUV index values.

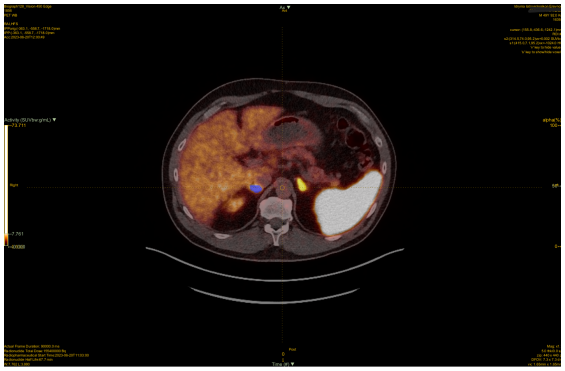

Figure 3.11: Axial view showing the ROIs in the adrenal glands on the PET/CT image.

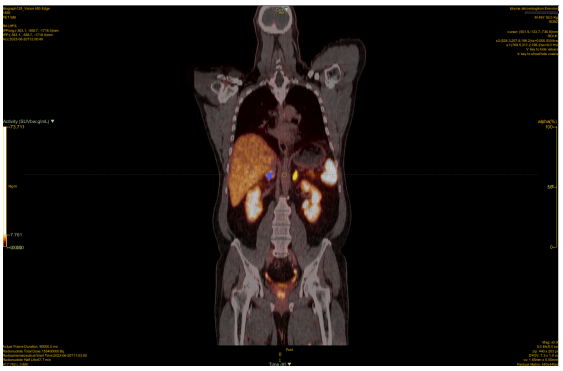

Figure 3.12: Saggital view showing the ROIs in the adrenal glands on the PET/CT image.

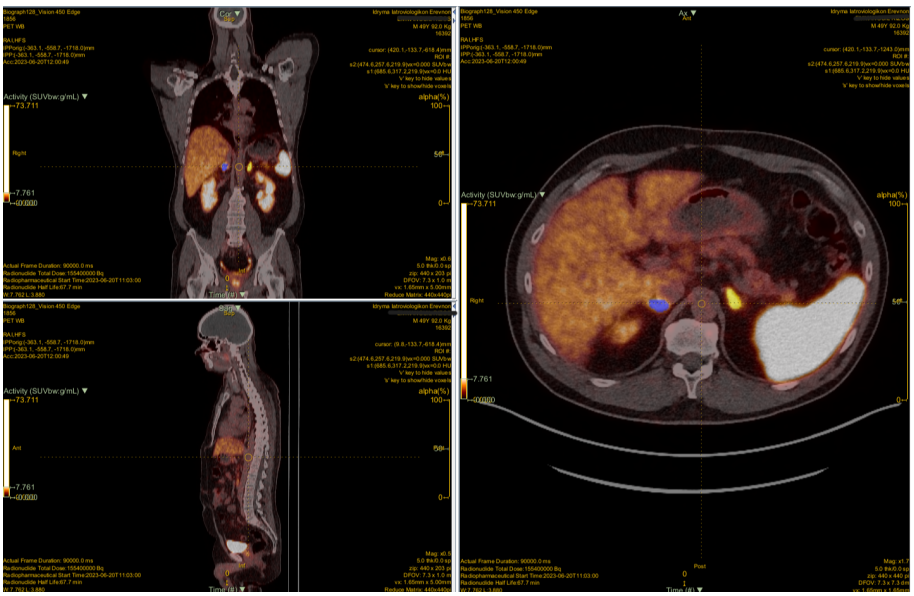

Figure 3.13: ROIs are mapped for adrenal glands on fused PET/CT images across all three projections.

Imaging alone often fails to provide specific characterization for adrenal lesions. Consequently, the ROI shape is not the only reliable dependable factor for diagnosis. Additional methods such as analyzing textural features, especially from PET images, can be employed. These features go beyond simple shape analysis and can provide more detailed and nuanced information for accurate diagnosis and characterization of lesions [58, 59].

3.4 Data - Statistical Analysis

We initiated our statistical analysis by focusing on the first two groups of patients, specifically examining the pituitary gland located within the cranial cavity and the adrenal glands to confirm our hypothesis. Our objective was to investigate the relationship between the SUV and the injected dose. We soon realised that there was no apparent correlation with either the injected activity or the patient's body weight (see Figures 3.14, 3.15, 3.19). Therefore, we attempted to classify the patients in six groups based on the fraction of injected activity per kilogram of tissue.

In Group 1, there were 18 patients with a fraction range of 0.82 to 1.99; Group 2 included 53 patients with a fraction range of 2.00 to 2.50; Group 3 comprised 41 patients with a fraction range of 2.51 to 3.00; Group 4 consisted of 28 patients with a fraction range of 3.01 to 3.50; Group 5 involved 11 patients with a fraction range of 3.51 to 4; and finally, Group 6 included 9 patients with a fraction range of 4.01 to 7.48.

			Group 1	**Group 2**	**Group 3**	**Group 4**	**Group 5**	**Group 6**
PITUITARY		Mean	3.02	3.06	3.24	3.38	2.65	3.52
		stdev	0.59	0.76	0.99	1.02	0.75	0.72
		Median	2.86	2.92	2.94	3.13	2.54	3.712
		Range	1.96-4.16	1.84-4.92	1.90-6.19	1.83-6.61	1.80-4.06	2.43-4.91
ADRENAL GLANDS	**LEFT**	Mean	9.84	9.96	9.98	9.47	8.55	10.80
		stdev	1.87	2.32	1.83	1.93	1.96	1.68
		Median	9.65	10.62	9.81	9.65	8.31	11.24
		Range	6.59-13.26	5.1-13.78	5.07-14.3	5.07-13.4	5.56-11.93	8.54-14.04
	RIGHT	Mean	9.41	9.20	9.42	8.69	8.11	9.96
		stdev	1.54	2.08	1.90	1.99	1.69	1.04
		Median	8.79	9.37	9.585	8.66	7.86	10.37
		Range	7.32-12.31	5.16-13.81	5.01-13.9	4.84-13.1	5.70-10.84	8.4-11.18

Table 3.3: Average,Median,Standard Deviation and Range of SUVmean across all Groups.

The various groups exhibit a spectrum of injected activity per kilogram of tissue . Upon analyzing each group individually, we observed that the average SUV_{mean} have a similar value across all groups, as shown in table 3.3. However, there is a notable standard deviation of approximately 20-30%, suggesting an inherent variability. This level of spread within the data set, is making it challenging to precisely determine the central tendency or make predictions based only on the mean value.

Despite this, we delved deeper by examining the extreme values of injected activity per kilogram of tissue to ascertain whether there is a correlation between the administered dose and the pituitary uptake. We reviewed both the lowest and highest administered doses. For patients with the two most extreme administered doses of radiopharmaceutical, it is revealing that: Patient No.140, who received a dosage of 0.82 MBq/kg, exhibited an SUV_{mean} of 3.22. In contrast, Patient No.109, administered with a dosage of 7.48 MBq/kg, showed a lower SUV_{mean} of 2.8 . Surprisingly, this does not show any apparent correlation between the administered dose and the SUV_{mean}.

This finding presents a paradoxical outcome, so then we tried to explore potential distinctions in patients based on gender. Given the crucial role of the pituitary as a neuroendocrine gland, which is affected by various influences, but in particular by hormonal activities, the following questions were our primary focus [43, 44].

1. Are the receptors identical across individuals?
2. Do receptors differ between males and females?
3. Is uptake in the pituitary ultimately independent of body weight or injected dose?

Furthermore, existing literature suggests that gland height may vary with both age and gender, due to the activity of the gland. This means that changes in pituitary size are likely to correspond to changes in the standardised uptake value (SUV) indices. These changes would be indicative of changes in glandular uptake, either increased or decreased, thus affecting SUV measurements. Therefore, we sought to clarify whether such discrimination exists in our patient group [43, 44]. So, we have divided our patients into two different groups.
The first group includes 81 female patients, while the second group includes 79 male patients. This division allows for a more focused analysis of potential gender-based

variations in our study parameters. Below, we present the table corresponding to the female and male groups.

	No. of patients	**Age**	**SUVmean**	**St.Dev**	**Median**	**Range**
Women	81	58±15	3.47	0.98	3.42	1.75-6.62
Men	79	60±13	2.83	0.62	2.73	1.84-4.91

Table 3.4: Groups based on genders

While the average age of women and men is very similar, the results revealed that women have a higher uptake of ^{68}Ga-DOTATOC in the pituitary region compared to men, with an average SUV_{mean} of 3.47 for women compared to 2.83 for men. This result is consistent with the literature, as women, due to their physiology, have elevated hormone levels related to fertility and menopause, while men, due to the absence of the ovulatory cycle and the delayed start of andropause, do not experience significant changes in their hormones and overall physiology. However, we cannot rely only on one parameter, as the differentiation of the SUV_{mean} index is not significant for all the above conditions we considered.

So, we proceeded our examination on the CT images to uncover the information they could provide. Our focus was on measuring the ***Hounsfield Units (HU)*** within the regions of interest. Hounsfield units are a measure of radiodensity. They indicate the degree of attenuation of x-rays as they pass through tissues, offering valuable information about tissue density and composition. The changes in tissue density observed on CT scans may indirectly reflect underlying biological processes, including cell proliferation. For example, areas of increased tissue density may indicate the presence of denser structures such as tumors, which could be associated with increased cell proliferation [60, 61]. The calculation of Hounsfield Units proved challenging, due to the fact that we conducted the procedure manually, and the exact identification of the organ under study became very difficult. It should be noted that we had to design new ROIs because CT and PET scans are never a perfect match.

Therefore, we needed to be very precise in our design due to the significant contrast in luminosity depending on the tissue type. In the case of the adrenal glands, a thorough attention to the drawing of the Region of Interest (ROI) was essential.

Even slight deviations from tissue boundaries could lead to dramatic fluctuations in Hounsfield Units. Any deviation from soft tissue would lead to excessively large negative values due to air attenuation. Concerning the pituitary gland, the ROI selection became even more challenging. This is because the gland is nearly transparent to x-rays. Consequently, the pituitary is not visible on CT imaging unless contrast material is administered. In our case, no contrast material was injected, resulting in minimal visualization of the pituitary on the CT images. This means that once again, disproportionately large negative values are observed.

We experimented with 35 patients to investigate weather there's a connection between *SUV* from PET images and the *Hounsfield Units* in both regions, pituitary and adrenal glands. Ultimately, we discovered that the values we received were not precise, leading us to consider designing new ROIs using machine learning for better results. However, this was not the scope of this study.

After all, our final consideration was to look closely at the textural features of the PET images. These patterns reveal details about how the radiopharmaceutical is being absorbed at a level that is not discernible otherwise. From LIFEx v7.4.0 we can extract over 200 textural features from PET images, leading us to gather these features individually for all three ROIs (R_1, R_2, R_3) from each of the 160 patients. We aim to identify a correlation between the SUV_{mean} and a certain number of textural features. Initially, we tried for a multi linear correlation, since there wass no clear dependence of SUV_{mean} on the injected dose (MBq).

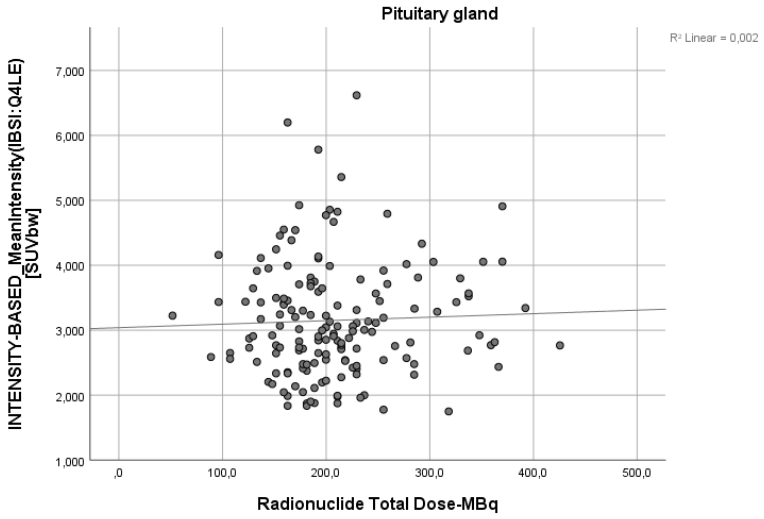

Figure 3.14: Plot of the SUVmean for pituitary gland.

As is apparent from the scatter plots in Figures 3.14, 3.15, 3.19, the regression line for the pituitary gland suggests a very weak correlation between the administered dose and the SUV mean. The coefficient of determination (R^2) indicates that only about 2% of the variance in SUV_{mean} can be explained by the administered dose. Overall, the data points appear to be widely scattered, suggesting a lack of strong correlation between these variables. Similar plots are observed in the adrenal glands, where the coefficient of determination is less than 5%.

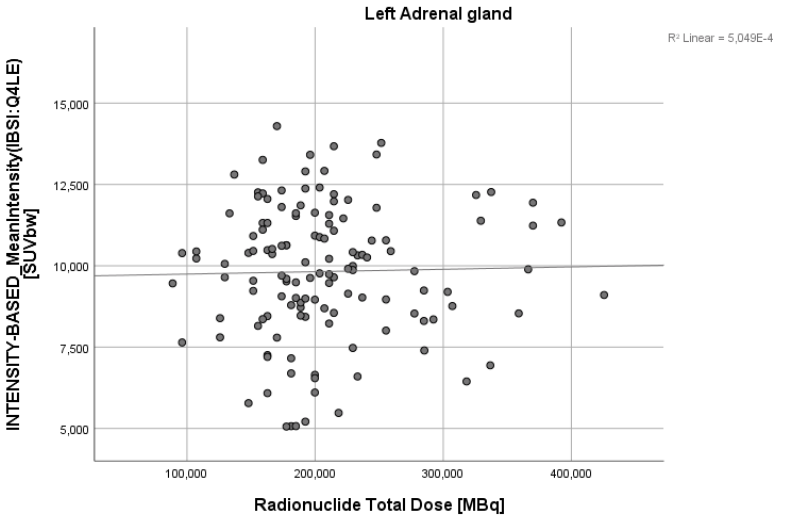

Figure 3.15: Plot of the SUVmean for the left adrenal gland.

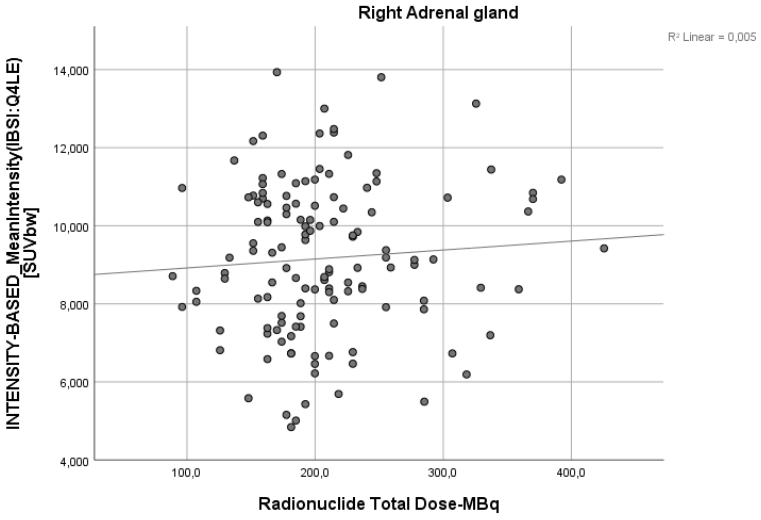

Figure 3.16: Plot of the SUVmean for the right adrenal gland.

Before we began our multiple linear regression analysis, we first checked for non-linear correlations using a Spearman test. Because the Spearman test gave us limited results with a correlation of 54%, we proceeded to multiple linear regression.

The first statistical procedure performed was to assess the normality of the SUV_{mean} which is the dependent variable, in both the pituitary and adrenal glands. We performed the Kolmogorov-Smirnov (K-S) test due to the large sample size. Assuming we have two cases. The first is that our sample comes from a population with a known distribution function $F_1(x)$, i.e. the normal distribution function.

- H_0: $F_X = F_1(X)$

The second is that, alternatively (alternative hypothesis) we should assume that our sample is not derived from the above function but from some other function.

- H_1: $F_X \neq \mathrm{F}_1(X)$

One-Sample Kolmogorov-Smirnov Test

		Pituitary gland	**Left Adrenal gland**	**Right adrenal gland**
N		160	129	129
Normal Parameters a,b	Mean	3.15	9.82	9.16
	Std. Dev	0.88	2.09	1.96
Most Extreme Differences	Absolute	0.09	0.04	0.06
	Positive	0.09	0.03	0.04
	Negative	-0.06	-0.04	-0.06
Test Statistic		0.09	0.04	0.06
Asymp. Sig. (2-tailed)		.006	.200	.200

Table 3.5: The table presents the normality K-S test

Since the p-value is greater than 0.05, then the initial hypothesis is accepted, 3.5 i.e. the random variable from which the sample under study came from, follows the normal distribution. Also, we conducted a test to assess the independence of the SUV_{mean} variable with the number of patients.

We noticed that, with few exceptions, the values typically fall within the range of 2 to 5 and are uniformly distributed across the number of patients for the pituitary. Similarly, for adrenal glands, the range extends from 6 to 14.

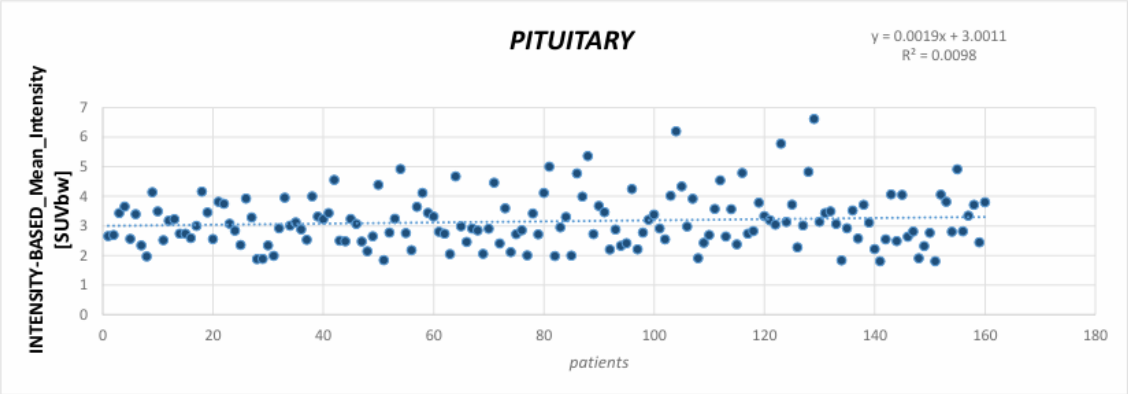

Figure 3.17: Plot of the SUVmean for pituitary gland

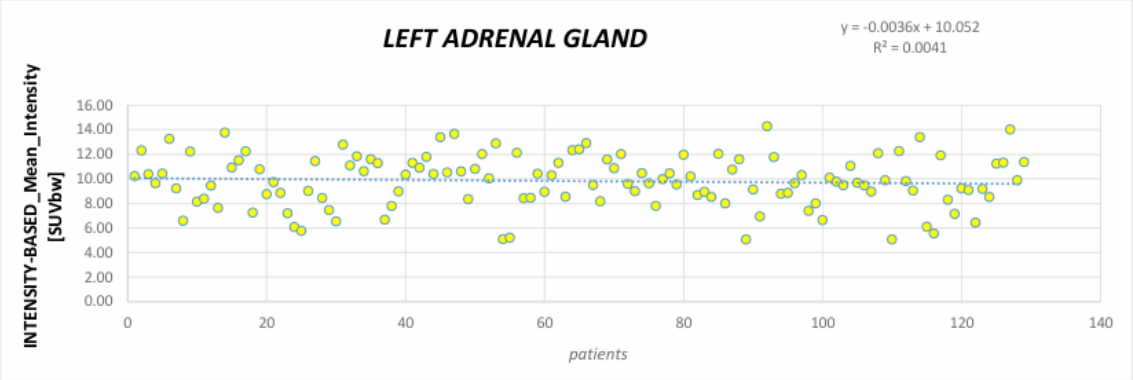

Figure 3.18: Plot of the SUVmean for left adrenal gland

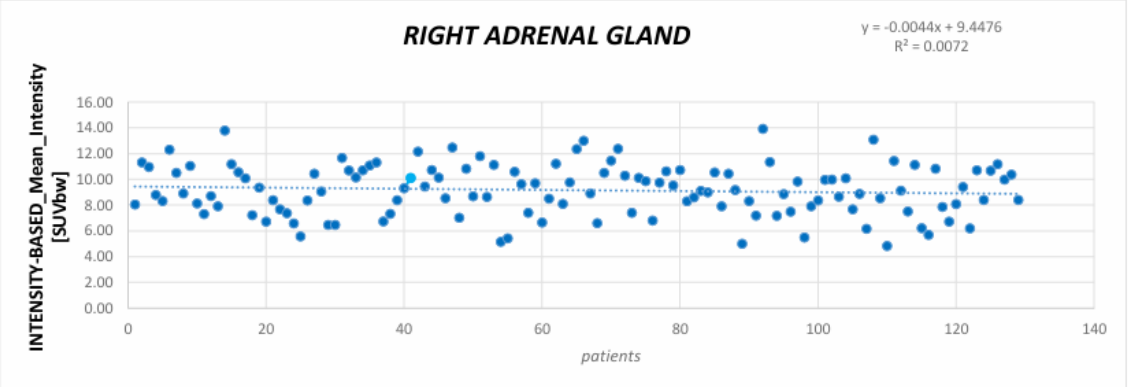

Figure 3.19: Plot of the SUVmean for right adrenal gland

Afterwards, we proceeded with running the multiple linear regression, aiming to predict the SUV_{mean} index using the values of the independent variables. The general equation of a multiple linear regression model with p independent variables

can be expressed as:

$$Y = \beta_0 + \beta_1 X_1 + \beta_2 X_2 + \ldots + \beta_p X_p + \varepsilon \ . \tag{3.1}$$

Y is the dependent variable (SUV_{mean}), X_1,X_2,...,X_p are the predictor variables, β_0 is the intercept (constant), β_1, β_2, β_p are the partial regression coefficients (parameters) associated with each independent variable and ε is the error term.

Regression Statistics	
Multiple R	0.99
R Square	0.97
Adj. R^2	0.97
Standard Error	0.15
Observations	160

Analysis of Variation				
	df	*SS*	*MS*	*F*
Regression	5.00	120.36	24.07	1067.98
Residual	154.00	3.47	0.02	
Total	159.00	123.83		

	Coefficients	*Standrad Error*	*t*	*P-value*
Intercept	1.15	0.181	6.332	2.51039E-09
SUV_{max}	0.07	0.024	3.051	0.002
COV	-1.60	0.261	-6.102	8.12557E-09
Energy	0.0006	3.72215E-05	14.999	6.35335E-32
$GLCM_{SumEntropy}$	-0.14	0.052	-2.567	0.011
$GLCM_{DifferenceEntropy}$	0.29	0.064	4.499	1.33662E-05

Table 3.6: Multiple Linear Regression of the Pituitary gland.

The R^2 indicates the proportion of how much of the variability in the data is

Regression Statistics	
Multiple R	0.98
R Square	0.96
Adj. R^2	0.96
Standard Error	0.36
Observations	132

Analysis of Variation				
	df	*SS*	*MS*	*F*
Regression	5.00	551.45	110.29	812.32
Residual	129	17.514	0.135	
Total	134	123.83		

	Coefficients	*Standrad Error*	*t*	*P-value*
Intercept	0.400	0.592	0.676	0.499793174
VOI	-0.0002	3.77185E-05	-7.187	4.73047E-11
SUV_{max}	0.372	0.020	17.821	1.35349E-36
COV	-18.190	0.784	-23.176	8.01141E-48
Energy	2.14496E-05	3.99339E-06	5.371	3.52581E-07
$GLCM_{DifferenceEntropy}$	0.906	0.084	10.697	1.65111E-19

Table 3.7: Multiple Linear Regression of the Left Adrenal gland.

captured by the model. Here, the models explain for all the regions of interest more than 95% of the data's variability, signifying strong explanatory power (see Figures 3.20, 3.21, 3.22). With observations exceeding 30, indicating a robust sample size, the significance F for the regression is 1.467E-117, which is well below the significance level of $\alpha = 0.01$, underscoring the model's effectiveness.

The coefficients in the regression model specify the relationship between the dependent (y) and the independent variables (x). A positive coefficient indicates

Regression Statistics				
Multiple R	0.97			
R Square	0.95			
Adj. R^2	0.95			
Standard Error	0.41			
Observations	132			
Analysis of Variation				
	df	*SS*	*MS*	*F*
Regression	5	470.45	94.09	553.80
Residual	126	21.40	0.169	
Total	131	491.86		
	Coefficients	*Standrad Error*	*t*	*P-value*
Intercept	-0.374	0.642	-0.583	0.560
VOI (mm^3)	-0.0003	4.38776E-05	-7.484	1.08742E-11
SUV_{max}	0.338	0.027	12.352	1.86329E-23
COV	-16.621	0.881	-18.856	1.70665E-38
Energy	2.62225E-05	6.16295E-06	4.254854429	4.04641E-05
$GLCM_{DifferenceEntropy}$	1.025	0.099	10.306	1.93909E-18

Table 3.8: Multiple Linear Regression of the Right Adrenal gland.

that as the independent variable increases, the dependent variable also tends to increase, suggesting a positive correlation between the two. On the contrary, a negative coefficient signifies that an increase in the independent variable is associated with a decrease in the dependent variable, implying an inverse relationship.

The p-value serves as an indicator of the significance of the coefficients in the regression model. If the p-value is below 0.05, it suggests that the coefficient is unlikely to be zero, and thus, the relationship between the variables is considered statistically

significant. This signifies that the coefficient provides meaningful information about the relationship between the variables in the model.

One noteworthy observation refers to the reduced number of observations for the adrenal glands (see Tables 3.7 and 3.8). Three pairs were excluded from the study with the intervention of the Radiologist, as it was noted that these pairs exhibited asymmetrical uptake in the right and left adrenal glands. Asymmetric uptake is considered when there is a disparity of more than 20% in the SUVmean between the right and left adrenal glands. This decision was made due to the possibility of underlying abnormalities. Based on Tables 3.6, 3.7 and 3.8 the following equations were constructed to describe the best possible regression model of SUV_{mean} for each region of interest. Namely, to construct a model that has the smallest possible number of independent variables.

Pituitary gland

$$\begin{aligned}\text{SUVmean} = {} & 1.15 + 0.07 \times \text{SUVmax} - 1.6 \times \text{COV} + 0.0006 \times \text{Energy} \\ & + 0.29 \times \text{GLCM\_DifferenceEntropy} - 0.14 \times \text{GLCM\_SumEntropy}\end{aligned} \quad \textbf{(3.2)}$$

Left Adrenal gland

$$\begin{aligned}\text{SUVmean} = {} & 0.4 - 0.0002 \times \text{VOI} + 0.372 \times \text{SUVmax} - 18.2 \times \text{COV} \\ & + 2.14 \times 10^{-5} \times \text{Energy} + 0.906 \times \text{GLCM\_DifferenceEntropy}\end{aligned} \quad \textbf{(3.3)}$$

Right Adrenal gland

$$\begin{aligned}\text{SUVmean} = {} & -0.374 - 0.0003 \times \text{VOI} + 0.338 \times \text{SUVmax} - 16.621 \times \text{COV} \\ & + 2.62 \times 10^{-5} \times \text{Energy} + 1.025 \times \text{GLCM\_DifferenceEntropy}\end{aligned} \quad \textbf{(3.4)}$$

The equations describe that the dependent variable, SUV_{mean}, is predicted by several independent variables. These independent variables include SUV_{max}, VOI, COV, $Energy$, $GLCM_{DifferenceEntropy}$, and $GLCM_{SumEntropy}$. The coefficients in front of each independent variable indicate the strength and direction of their relationship with SUV_{mean}.

Below are the scatter plots (see Figures 3.20, 3.21, 3.22) that illustrate the relationship between the dependent variable (SUVmean) and the unstandardized predicted value obtained from multiple independent variables using the MLR model.

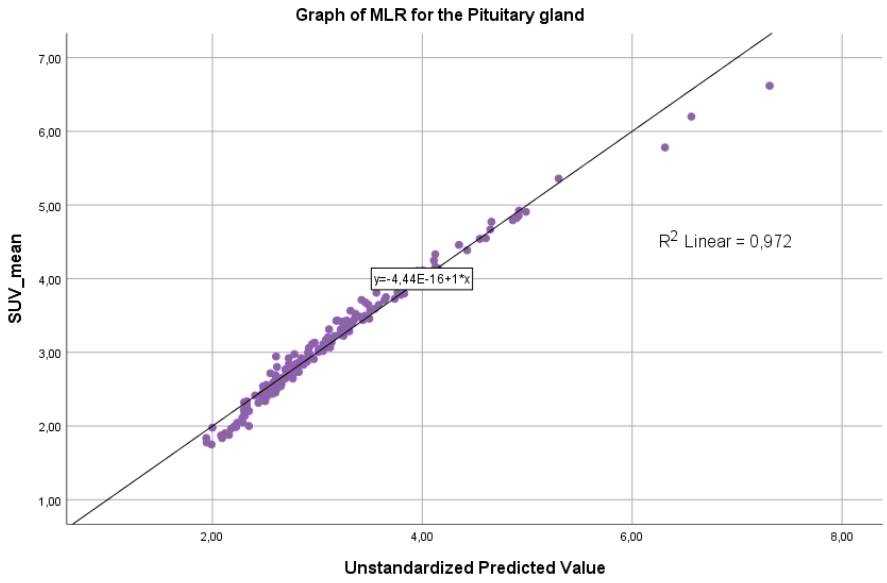

Figure 3.20: Plot of the MLR for pituitary gland

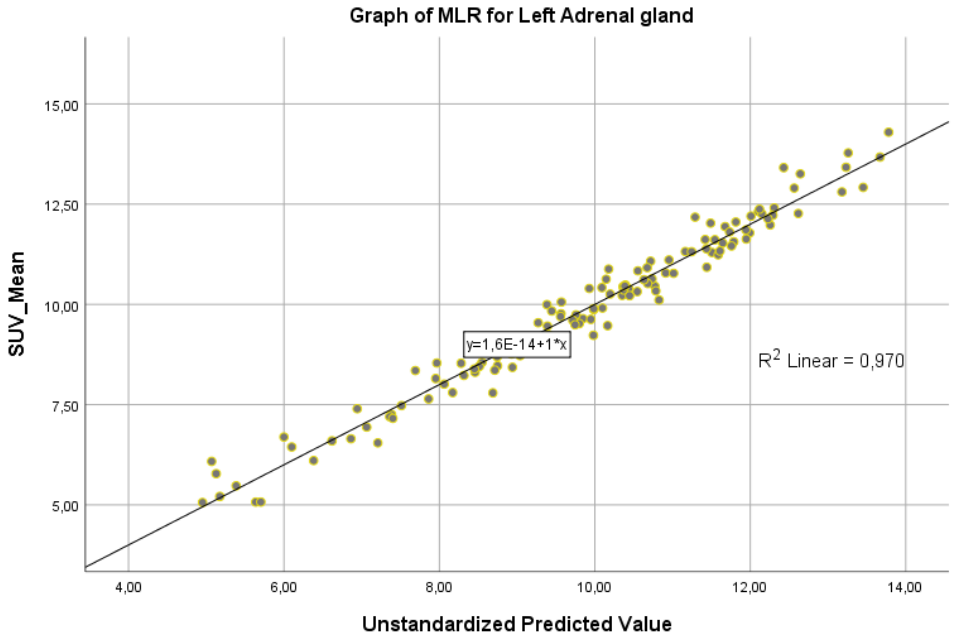

Figure 3.21: Plot of the MLR for left adrenal gland

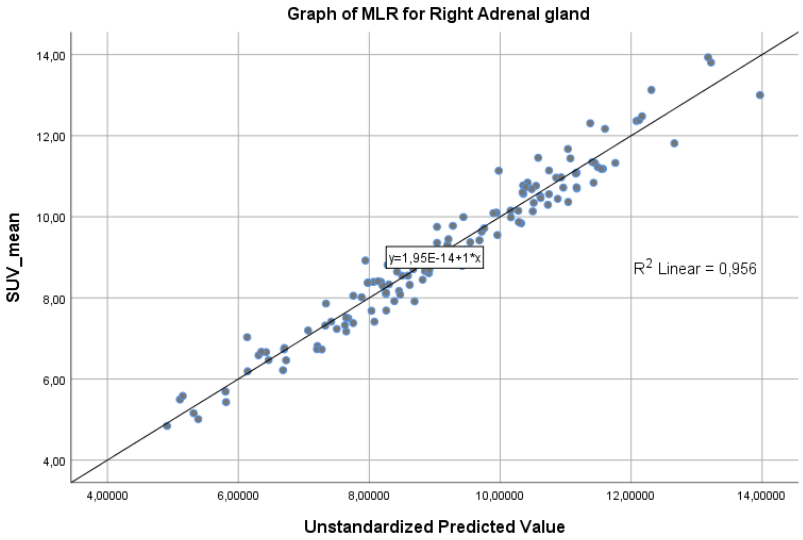

Figure 3.22: Plot of the MLR for right adrenal gland

Indeed, the equations reveal that the COV possesses the highest factor among all the parameters considered in the model for each ROI. This implies that COV exhibits the most significant correlation with the SUVmean outcome relative to the other variables.

COV is the quantitative variability of the SUV_{mean} within the volume of interest, and after closer examination of the COV values it becomes evident that there is consistency and stability in the numerical results, especially for the pituitary gland. The consistency in numerical outcomes allows acurate prediction of somatostatin receptors uptake, a critical factor in forecasting patient SUV_{mean} to ^{177}Lu-DOTATOC therapy.

Descriptive Statistics	N	Range	Minimum	Maximum	Mean	Std. Dev
PITUITARY_COV	160	0.333	0.28	0.614	0.449	0.061
LEFT ADRENAL GLAND_COV	132	0.298	0.191	0.489	0.296	0.062
RIGHT ADRENAL GLAND_COV	132	0.272	0.19	0.462	0.299	0.064
Valid N (listwise)	132					

Table 3.9: Description of COV statistics.

3.5 Discussion

This study aims to evaluate the uptake of ^{68}Ga-DOTATOC (SUV_{mean}) in the pituitary region to assess somatostatin receptors and correlate this uptake with treatment response to ^{177}Lu-DOTATOC. When characterizing and comparing somatostatin receptors in the adrenal glands with those in the brain's pituitary region, it was observed that accuracy in hypothesis-testing differed between the two anatomical sites. Specifically, the variability in the VOI for adrenal glands across different patients, owing to anatomical differences, resulted in a wider distribution of somatostatin receptors and subsequently higher SUV_{mean} values. Conversely, the VOI for the pituitary region remained consistent among patients, leading to more precise measurements and a standard deviation of approximately 13% for COV reflecting somatostatin receptors.

This agreement supports the initial hypothesis that the pituitary gland owns a specific quantity of receptors, and saturation of these receptors by the radiopharmaceutical leads to no further uptake in that area. The inclusion of adrenal glands in the analysis served as a means of verification, revealing alignment with the initial hypothesis, although with additional considerations due to anatomical variations. With the assistance of textural analysis, several advantages emerge in this framework. Firstly, it is a noninvasive technique that doesn't necessitate additional scans, thereby minimizing patient risk, reducing costs and radiation exposure. By using these benefits, texture analysis emerges as a valuable tool for evaluating somatostatin receptor uptake patterns, aiding in both diagnosis and treatment planning.

Notably, uptake in the pituitary and adrenal glands is expected to be both physiological and consistent due to their inherent expression of SSTRs [48, 57]. According to this article [62], a linear estimation method correlates the mean standardized uptake value (SUV_{mean}) of ^{68}Ga-DOTATOC with the absorbed dose per administered activity (^{177}Lu-DOTATATE). Therefore, it can be asserted that if the mean standardized uptake value in a healthy organ within the neuroendocrine system remains constant, the corresponding region of interest will exhibit stability throughout Lutetium treatment. As a result, the tissue or organ can be regarded as safe for radio-therapeutic procedures, providing valuable insights that underscore the significance of monitoring SUV_{mean} in assessing the safety and efficacy of targeted PRRTs [62].

3.6 Conclusion

Our research revealed that an important parameter from the textural analysis of ^{68}Ga-DOTATOC PET/CT images is the Coefficient of Variation (CoV), which allows the assessment of the variability of uptake in normal, healthy somatostatin receptors at different anatomical regions. This suggests that the difference in absorption of radioactive uptake correlates with the variability in somatostatin receptors (SSTR), potentially indicating differences in receptor quantity or distribution within neuroendocrine tissue [48].

The CoV consistently maintains a value close to 0.45 for the pituitary, with a standard deviation of 0.06, corresponding to approximately 13% variability. This implies that the variable can be considered stable, indicating a consistent level of heterogeneity among the receptors within healthy tissues. Therefore, if there is a stable number of receptors in healthy tissues, during PRRT treatment, there will also be a consistent uptake in these structures. This is because all receptor sites in these structures will have been occupied.

Bibliography

[1] DL Bailey et al. "Nuclear Medicine Physics: A Handbook for Teachers and Students. Endorsed by: American Association of Physicists in Medicine (AAPM), Asia–Oceania Federation of Organizations for Medical Physics (AFOMP), Australasian College of Physical Scientists and Engineers in Medicine (ACPSEM), European Federation of Organisations for Medical Physics (EFOMP), Federation of African Medical Physics Organisations (FAMPO), World Federation of Nuclear Medicine and Biology (WFNMB)". In: (2014).

[2] Qihui Lyu, Ryan Neph, and Ke Sheng. "Pair production tomography imaging". In: (2021).

[3] David W Townsend. "Basic science of PET and PET/CT". In: *Positron Emission Tomography: Clinical Practice*. Springer, 2006, pp. 1–16.

[4] Thomas Carlier et al. "From a PMT-based to a SiPM-based PET system: a study to define matched acquisition/reconstruction parameters and NEMA performance of the Biograph Vision 450". In: *EJNMMI physics* 7 (2020), pp. 1–16.

[5] Vanessa Nadig et al. "Hybrid total-body pet scanners—current status and future perspectives". In: *European journal of nuclear medicine and molecular imaging* 49.2 (2022), pp. 445–459.

[6] J Ouyang and G El Fakhri. "Quantitative Nuclear Medicine. Chapter 17". In: (2014).

[7] Timothy G Turkington. "Introduction to PET instrumentation". In: *Journal of nuclear medicine technology* 29.1 (2001), pp. 4–11.

[8] John M Ollinger. "Model-based scatter correction for fully 3D PET". In: *Physics in Medicine & Biology* 41.1 (1996), p. 153.

[9] Charles C Watson, DMEC Newport, and Mike E Casey. "A single scatter simulation technique for scatter correction in 3D PET". In: *Three-dimensional image reconstruction in radiology and nuclear medicine*. Springer, 1996, pp. 255–268.

[10] BM Mazoyer, MS Roos, and RH Huesman. "Dead time correction and counting statistics for positron tomography". In: *Physics in Medicine & Biology* 30.5 (1985), p. 385.

[11] MK Singh. "A review of digital PET-CT technology: comparing performance parameters in SiPM integrated digital PET-CT systems". In: *Radiography* 30.1 (2024), pp. 13–20.

[12] M Defrise et al. "A normalization technique for 3D PET data". In: *Physics in Medicine & Biology* 36.7 (1991), p. 939.

[13] Lampros Theodorakis et al. "A review of PET normalization: striving for count rate uniformity". In: *Nuclear medicine communications* 34.11 (2013), pp. 1033–1045.

[14] Anthony D Wrixon. "New ICRP recommendations". In: *Journal of radiological protection* 28.2 (2008), p. 161.

[15] S Mattsson et al. "ICRP publication 128: radiation dose to patients from radiopharmaceuticals: a compendium of current information related to frequently used substances". In: *Annals of the ICRP* 44.2_suppl (2015), pp. 7–321.

[16] Y Yonekura et al. "ICRP publication 127: radiological protection in ion beam radiotherapy". In: *Annals of the ICRP* 43.4 (2014), pp. 5–113.

[17] SC Strother, ME Casey, and EJ Hoffman. "Measuring PET scanner sensitivity: relating countrates to image signal-to-noise ratios using noise equivalents counts". In: *Ieee transactions on nuclear science* 37.2 (1990), pp. 783–788.

[18] Timothy R DeGrado et al. "Performance characteristics of a whole-body PET scanner". In: *Journal of Nuclear Medicine* 35.8 (1994), pp. 1398–1406.

[19] Magnus Dahlbom. "PET Calibration, Acceptance Testing, and Quality Control". In: *Basic Science of PET Imaging* (2017), pp. 229–255.

[20] Tom Sanderson et al. “Underestimation of 68Ga PET/CT SUV caused by activity overestimation using default calibrator settings”. In: *Physica Medica* 59 (2019), pp. 158–162.

[21] Joyce Van Sluis et al. “Performance characteristics of the digital biograph vision PET/CT system”. In: *Journal of Nuclear Medicine* 60.7 (2019), pp. 1031–1036.

[22] Alejandra Valladares, Thomas Beyer, and Ivo Rausch. “Physical imaging phantoms for simulation of tumor heterogeneity in PET, CT, and MRI: an overview of existing designs”. In: *Medical physics* 47.4 (2020), pp. 2023–2037.

[23] Catherine M Lockhart et al. “Quantifying and reducing the effect of calibration error on variability of PET/CT standardized uptake value measurements”. In: *Journal of Nuclear Medicine* 52.2 (2011), pp. 218–224.

[24] Darrin W Byrd et al. “Evaluation of cross-calibrated 68Ge/68Ga phantoms for assessing PET/CT measurement bias in oncology imaging for single-and multicenter trials”. In: *Tomography* 2.4 (2016), pp. 353–360.

[25] Ute Hennrich and Martina Benešová. “[68Ga] Ga-DOTA-TOC: the first FDA-approved 68Ga-radiopharmaceutical for PET imaging”. In: *Pharmaceuticals* 13.3 (2020), p. 38.

[26] Sophia Koukouraki et al. “Evaluation of the pharmacokinetics of 68 Ga-DOTATOC in patients with metastatic neuroendocrine tumours scheduled for 90 Y-DOTATOC therapy”. In: *European journal of nuclear medicine and molecular imaging* 33 (2006), pp. 460–466.

[27] Pat Zanzonico. “Positron emission tomography: a review of basic principles, scanner design and performance, and current systems”. In: *Seminars in nuclear medicine*. Vol. 34. 2. WB Saunders. 2004, pp. 87–111.

[28] Irina Velikyan. “Prospective of 68Ga-radiopharmaceutical development”. In: *Theranostics* 4.1 (2014), p. 47.

[29] Shady Hermena and Michael Young. “CT-scan image production procedures”. In: (2021).

[30] Lee W Goldman. “Principles of CT and CT technology”. In: *Journal of nuclear medicine technology* 35.3 (2007), pp. 115–128.

[31] Radiological Protection. "ICRP publication 103". In: *Ann ICRP* 37.2.4 (2007), p. 2.

[32] Sara Massironi et al. "Neuroendocrine tumors of the gastro-entero-pancreatic system". In: *World journal of gastroenterology: WJG* 14.35 (2008), p. 5377.

[33] MU Khan et al. "Clinical indications for gallium-68 positron emission tomography imaging". In: *European Journal of Surgical Oncology (EJSO)* 35.6 (2009), pp. 561–567.

[34] Lucia Martiniova et al. "Gallium-68 in medical imaging". In: *Current radiopharmaceuticals* 9.3 (2016), pp. 187–207.

[35] Sangeeta Ray Banerjee and Martin G Pomper. "Clinical applications of Gallium-68". In: *Applied Radiation and Isotopes* 76 (2013), pp. 2–13.

[36] Michael K. Schultz. "Theranostics, Gallium-68, and Other Radionuclides: A Pathway to Personalized Diagnosis and Treatment". In: *Journal of Nuclear Medicine* 54.4 (2013), pp. 659–660. ISSN: 0161-5505. DOI: 10.2967/jnumed.113.121350. eprint: https://jnm.snmjournals.org/content/54/4/659.2.full.pdf. URL: https://jnm.snmjournals.org/content/54/4/659.2.

[37] EMA Europa. "SomaKit TOC : EPAR - Product Information(N/0027)". In: *SUMMARY OF PRODUCT CHARACTERISTICS* 35 (29 September 2023). URL: https://www.ema.europa.eu/en/documents/product-information/somakit-toc-epar-product-information_en.pdf,.

[38] Shawna L. Rego et al. "CARE Dose4D CT Automatic Exposure Control System". In: *Radiological Society of North America(RSNA), Mayo Foundation for Medical Education and Research* (2007), p. 1.

[39] Katharine Grant and Rainer Raupach. "SAFIRE: Sinogram affirmed iterative reconstruction". In: *Whitepaper, Siemens AG* (2012).

[40] Thorsten D Poeppel et al. "68Ga-DOTATOC versus 68Ga-DOTATATE PET/CT in functional imaging of neuroendocrine tumors". In: *Journal of nuclear medicine* 52.12 (2011), pp. 1864–1870.

[41] Pedro Iglesias, Jorge Cardona, and Juan José Díez. "The pituitary in nuclear medicine imaging". In: *European Journal of Internal Medicine* 68 (2019), pp. 6–12.

[42] HM Roppolo et al. "Normal pituitary gland: 1. Macroscopic anatomy-CT correlation." In: *American journal of neuroradiology* 4.4 (1983), pp. 927–935.

[43] SB Brown, Kathleen Murphy Irwin, and DR Enzmann. "CT characteristics of the normal pituitary gland". In: *Neuroradiology* 24 (1983), pp. 259–262.

[44] RG Peyster et al. "CT of the normal pituitary gland". In: *Neuroradiology* 28 (1986), pp. 161–165.

[45] Murat Fani Bozkurt et al. "Guideline for PET/CT imaging of neuroendocrine neoplasms with 68 Ga-DOTA-conjugated somatostatin receptor targeting peptides and 18 F–DOPA". In: *European journal of nuclear medicine and molecular imaging* 44 (2017), pp. 1588–1601.

[46] Michael A Blake and Giles Boland. *Adrenal imaging*. Springer Science & Business Media, 2009.

[47] Gurinder Nandra et al. "Technical and interpretive pitfalls in adrenal imaging". In: *Radiographics* 40.4 (2020), pp. 1041–1060.

[48] Rosa Fonti et al. "Heterogeneity of SSTR2 expression assessed by 68Ga-DOTATOC PET/CT using coefficient of variation in patients with neuroendocrine tumors". In: *Journal of Nuclear Medicine* 63.10 (2022), pp. 1509–1514.

[49] Christophe Nioche et al. "LIFEx: a freeware for radiomic feature calculation in multimodality imaging to accelerate advances in the characterization of tumor heterogeneity". In: *Cancer research* 78.16 (2018), pp. 4786–4789.

[50] C Nioche, F Orlhac, and I Buvat. "Texture User Guide, Local image features extraction". In: *LIFEx* 9 (2021).

[51] C Nioche, F Orhlac, and I Buvat. "Local Image Feature Extraction–LIFEx". In: *User Guide* (2023).

[52] A Zwanenburg et al. "The image biomarker standardisation initiative—IBSI 0.0. 1dev documentation 2019". In: *ProQuest Number: INFORMATION TO ALL USERS* ().

[53] Ruijiang Li et al. *Radiomics and Radiogenomics Technical Basis and Clinical Applications*. Mar. 2021, p. 484. ISBN: 9780367779580.

[54] Robert J Gillies, Paul E Kinahan, and Hedvig Hricak. "Radiomics: images are more than pictures, they are data". In: *Radiology* 278.2 (2016), pp. 563–577.

[55] V Prasad and RP Baum. "Biodistribution of the Ga-68 labeled somatostatin analogue DOTA-NOC in patients with neuroendocrine tumors: characterization of uptake in normal organs and tumor lesions". In: *QJ Nucl Med Mol Imaging* 54.1 (2010), pp. 61–67.

[56] A Kroiss et al. "68 Ga-DOTA-TOC uptake in neuroendocrine tumour and healthy tissue: differentiation of physiological uptake and pathological processes in PET/CT". In: *European journal of nuclear medicine and molecular imaging* 40 (2013), pp. 514–523.

[57] Rudolf A Werner et al. "Impact of tumor burden on quantitative [68 Ga] DOTATOC biodistribution". In: *Molecular Imaging and Biology* 21 (2019), pp. 790–798.

[58] Michael A Blake, Priyanka Prakash, and Carmel G Cronin. "PET/CT for adrenal assessment". In: *American Journal of Roentgenology* 195.2 (2010), W91–W95.

[59] Michael A Blake, Carmel G Cronin, and Giles W Boland. "Adrenal imaging". In: *American Journal of Roentgenology* 194.6 (2010), pp. 1450–1460.

[60] Tami D DenOtter and Johanna Schubert. "Hounsfield unit". In: (2019).

[61] Satoshi Nakasu et al. "CT Hounsfield unit is a good predictor of growth in meningiomas". In: *Neurologia medico-chirurgica* 59.2 (2019), pp. 54–62.

[62] Ragnar Bruvoll et al. "Correlations between [68Ga] Ga-DOTA-TOC uptake and absorbed dose from [177Lu] Lu-DOTA-TATE". In: *Cancers* 15.4 (2023), p. 1134.

[63] K. Henrichs. "The pituitary in nuclear medicine imaging". In: *Radiation Protection Dosimetry* 144 (Oct. 2019). DOI: 10.1016/j.ejim.2019.08.008. URL: https://www.sciencedirect.com/science/article/abs/pii/S0953620519302936?via%3Dihub.

[64] Kristen M. Waterstram-Rich Paul E. Christian. *Nuclear Medicine and PET/CT: Technology and Techniques*. 7th. ELSEVIER MOSBY, 2011. ISBN: 0323071929; 978-0323071925.

[65] Roberts S.B. Beanlands Richard L. Wahl. *Principles and Practice of PET and PET/CT*. 2nd ed. Lippincott Williams & Wilkins, 2008. ISBN: 9780781779999; 978-0781779999.

[66] R.Griffith et al. *ICRU Report 69 Direct Determination of the Body Content of Radionuclides*. Jan. 2003. ISBN: 1 870965 95 7.